BANDGAP FORMATION AND TUNING IN STIMULI-RESPONSIVE HYDROGEL-BASED PERIODIC STRUCTURES

A Thesis
Presented to
The Academic Faculty

By

Herit Patel

In Partial Fulfillment
of the Requirements for the Degree
Master of Science in the
George W. Woodruff School of Mechanical Engineering

Georgia Institute of Technology

May 2021

BANDGAP FORMATION AND TUNING IN STIMULI-RESPONSIVE HYDROGEL-BASED PERIODIC STRUCTURES

Thesis committee:

Dr. Alper Erturk, Advisor
School of Mechanical Engineering
Georgia Institute of Technology

Dr. Yuhang Hu, Co-Advisor
School of Mechanical Engineering
Georgia Institute of Technology

Dr. Karim Sabra
School of Mechanical Engineering
Georgia Institute of Technology

Date approved: April 20, 2021

ACKNOWLEDGMENTS

First and foremost, I would like to offer my sincerest gratitude to my advisors, Dr. Alper Erturk and Dr. Yuhang Hu, for providing me with the opportunity to work on this amazing research project. I will always be grateful for their guidance and advice towards this project. I would also like to thank Dr. Karim Sabra, for taking the time to be a part of the thesis reading committee and providing helpful insights into this work.

I would also like to thank all the past and present members of the Smart Structures and Dynamical Systems Laboratory as well as the Chemomechanics of Soft Materials Laboratory at Georgia Tech, who assisted me with numerous tasks ranging from setting up experiments to debugging models. I learnt a lot from our day to day interactions and group meetings. I would especially like to thank Jiehao Chen for his guidance and for developing the hydrogel samples and assisting me with the vibration experiments.

Finally, I would like to thank my parents, family, and friends for their constant support and encouragement.

TABLE OF CONTENTS

LIST OF TABLES

LIST OF FIGURES

SUMMARY

Over the past two decades, researchers have studied elastic/acoustic metamaterials and phononic crystals to enable certain structural properties that are not found in ordinary materials. One such property is the formation of a bandgap (a frequency range in which wave propagation is forbidden) to attenuate structural vibrations or noise over a desired frequency band. Metastructures, which are finite periodic structures with specified boundary conditions, can exhibit bandgap formation via geometry and/or material periodicity (Bragg scattering-based) or via resonating unit cells (locally resonant). The efforts presented in this thesis focus on the former approach in stimuli-responsive hydrogels which can achieve reprogrammable geometric and material periodicity through periodic swelling. Hydrogels are soft materials primarily composed of a network of hydrophilic polymers and water molecules. Many hydrogels have been made stimuli-responsive that can swell or shrink upon exposure to external triggers such as light radiation, relative humidity, temperature, etc. Because of their biocompatibility, hydrogels have been used extensively in many biomedical applications such as artificial organs, cell culture scaffolds, wound dressings, and drug carriers. Furthermore, hydrogels exhibit less internal damping compared to commonly used soft materials, offering a potential for structural dynamics and wave propagation applications. This work intends to study the use of hydrogels as metamaterials for bandgap formation and tuning due to their stimuli responsive behavior. This thesis first utilizes the transfer matrix method to perform the band structure (dispersion) analyses on unit cells of periodic hydrogel structures. In addition, finite structure frequency response analyses are performed using the finite element method. These models are then experimentally validated for hydrogel-based periodic cantilever beam configurations conducted on leucohydroxide (concentration is directly proportional to periodic swelling) based photo-responsive hydrogels. The effects of various parameters, such as unit cell length ratio and leucohydroxide concentration on bandgap and its tuning are further explored and ex-

perimentally validated. Both model simulations and experimental results suggest that increase in unit cell length ratio reduces both the center frequency and width of the bandgap, whereas higher leucohydroxide concentrations result in wider bandgaps at lower center frequencies.

CHAPTER 1
INTRODUCTION AND BACKGROUND

1.1 Bandgap Formation in Metamaterials

Vibrations can be destructive to many structures, hence it is necessary to attenuate the structural response to ensure safety and performance. Vibration attenuation can be achieved by adding damping to the structure. While this is a commonly employed approach, it could prove to be an expensive one and may require addition of bulky attachments like tuned mass dampers. By enabling bandgap formation, metamaterials and phononic crystals provide an innovative approach to attenuate structural vibrations or noise over a desired frequency band. A bandgap is a frequency range over which wave propagation is forbidden. Metamaterials can exhibit bandgap formation via geometric and/or material periodicity (Bragg-scattering based) or resonating unit cells (locally resonant). Bragg-scattering based bandgaps occur at wavelengths which are on the order of the lattice size of the crystal, hence large unit cells in conventional materials are required to create bandgaps at lower frequencies [1]. On the other hand, locally resonating metamaterials can create bandgaps at wavelengths much larger than the lattice size [2, 3]. Researchers have further studied coupled periodic and locally resonant metamaterials which can further enhance both the locally resonant and Bragg-scattering based bandgap width [4].

1.2 Wave Propagation in Periodic Structures

A periodic structure is a regular and repeating arrangement of atoms, particles, or unit cells. These structures can be artificially made or can exist in nature over a wide range of length scales. The size of the structures which possess periodicity can range from microscopic lumped diatomic systems such as crystal lattices [5] to multi-storey buildings,

bridges, etc. Over the past few decades, researchers have exploited structural periodicity to generate bandgaps and tune them over a desired frequency range. Research on periodic chains of masses and springs dates back to Newton and Lord Rayleigh [6]. Brillouin provided a comprehensive historical background and motivation to study wave propagation in periodic structures [1]. Bandgap formation in periodic continuous systems has also been studied in detail [7, 8]. Several innovative techniques such as placement of periodic inclusions, geometric, and material periodicities have been further explored to introduce bandgaps in structures. Depending on the design of these inclusions, geometric, and material periodicities, researchers have been able to design structures with bandgaps over desired frequencies [9].

1.3 Bandgap Tunability

Based on design specifications, metamaterials would be required to attenuate vibration or noise over a specific frequency band. Several innovative and efficient approaches have been recently developed to tune bandgaps in metamaterials. In recent years, researchers have studied metamaterial beams which can tune their bandgaps based on temperature based Young's moduli variations in shape memory alloy resonators [10, 11]. Researchers have also been able to develop bandgap tuning techniques in metamaterial structures via electromechanical/piezoelectric resonators [12–14]. Electro-mechanical resonators can provide a digital approach to instantaneously program bandgap without physically altering the structure [14]. Researchers have developed metamaterials with linear and non-linear bistable mechanical attachments which can possess wider bandgaps [15–17]. Additionally, bandgap tuning in acoustic metamaterials via both mechanical [18] and electro-mechanical [19] means has also been studied extensively. Several other innovative approaches such as tuning via magnetic field variation and periodic buckling in undulate beams have also been explored [20, 21].

Majority of bandgap formation and tuning studies have been conducted on structures

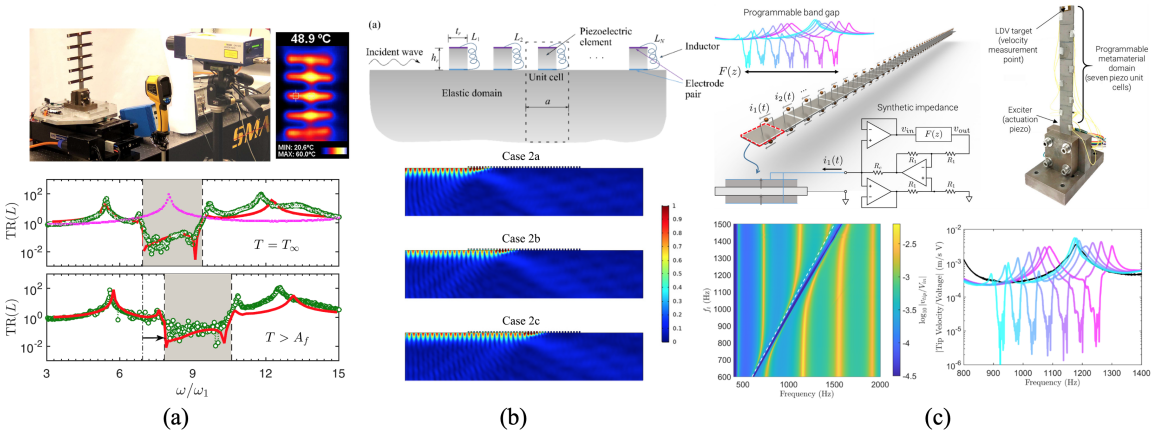

Figure 1.1: Different techniques used for bandgap tuning in metamaterials- (a) shape memory based locally resonant metamaterials [11] (b) piezoelectric circuit based tunable surface acoustic wave bandgaps [19] (c) piezoelectric based tunable bandgaps in flexural beams [14].

made from hard materials. On the contrary, this thesis seeks to examine the feasibility of bandgap formation in hydrogel-based metamaterials which are very soft in nature. Additionally, the stimuli-responsive behavior of hydrogels is utilized to induce physical changes in the structure which can ultimately provide an interesting and innovative approach for tuning bandgaps in hydrogel-based metamaterials.

1.4 Stimuli-Responsive Hydrogels

In recent years, hydrogels have been extensively studied due to their versatile range of biomedical applications, ranging from drug carriers to tissue engineering [22, 23]. Hydrogels are soft materials primarily composed of hydrophilic polymeric network and water molecules. These hydrogels can change their volume by absorbing or repelling water through chemical and/or physical means [24, 25]. Such change in volume can alter hydrogel mechanical properties such as density, modulus, diffusivity, and internal damping [26]. Recent studies have also shown that hydrogels possess less internal damping when compared to commonly used soft materials [27]. Such special property can be utilized in numerous structural dynamics and wave propagation applications.

Hydrogels have been made responsive to a variety of different environmental cases such as temperature, pH, electric field, light etc [28–31]. Among various stimuli-responsive hydrogels, photo-chemical hydrogels have the best spatial temporal control. However, the most conventional photo-chemical hydrogels require constant light radiation exposure to maintain its activated/swollen state [32]. In efforts to address this problem, recently, a leucohydroxide-based photo-responsive hydrogel, with decoupled light activation and swelling processes has been developed [33]. These hydrogels can obtain high deformation/swelling while maintaining good structural integrity. Additionally, the good spatial and temporal resolutions of these hydrogels pave the way for creating hydrogels with localized and periodic swelling which can be utilized to study bandgap formation and tuning in hydrogel-based metamaterials.

1.5 Outline of the Thesis

This work explores the bandgap formation and tuning in stimuli-responsive hydrogel-based periodic structures. Chapter 2 focuses on the dispersion analysis based approach for studying the bandgap formation. Dispersion analysis relates wavenumber, k, of a wavevector to its frequency, ω. Transfer matrix method is utilized to relate the forces and displacements at the boundaries of the unit cell of an infinite periodic structure to ultimately define the eigenvalue problem which can then be used to create the dispersion curves. Both Euler-Bernoulli and Timoshenko beam theories are considered to model the bandgap formation in periodic structures under bending vibrations. The variation in bandgap width and center frequency is evaluated with respect to changes in diameter, Young's modulus, and unit cell length ratio. Chapter 3 discusses the development and utilization of finite element method based frequency response analysis to study bandgap formation in periodic structures with finite number of unit cells. Hamilton's principle is used to create the finite element mass and stiffness matrices for Euler-Bernoulli and Timoshenko beam models. Cantilever boundary conditions are considered in the model and similar case studies (di-

ameter, Young's Modulus, and length ratio) are again repeated in this chapter. Chapter 4 discusses the experimental results from the shaker vibration tests which are performed on leucohydroxide based photo-responsive periodic hydrogels. Static deflection due to gravity is considered using a COMSOL model to ensure a good match with experimental results. Hydrogel samples with different leucohydroxide concentrations and length ratios are tested to evaluate changes in the location and width of bandgap. Chapter 5 concludes the findings and provides further recommendations for future work in this field.

CHAPTER 2
DISPERSION (BAND STRUCTURE) ANALYSIS

This chapter presents the dispersion-analysis-based efforts used to predict and tune the bandgap in a hydrogel structure with certain material and geometric periodicity. For any given structure, dispersion analysis relates wavenumber, k of a wavevector to its frequency, ω. Bandgap formation is first studied in diatomic chain model which is the simplest representation of periodic hydrogels studied in this work. Unit-cell-based dispersion relations are further established using transfer matrix method for axial, torsional, and flexural/bending modes of wave propagation. For bending modes, Timoshenko beam model is also developed alongside Euler-Bernoulli beam model to account for shear deformation and rotational inertia which can be significant in soft structures such as hydrogels. Several case studies for bending models are also presented here to describe how bandgap width and center frequency vary with respect to the extent of geometric and material periodicity.

2.1 Diatomic Chain Model

A periodic repetition of geometry or material property such as Young's modulus in a structure results in local mass and stiffness variation. The extent of this variation is what ultimately controls the quality of bandgap. A diatomic chain as shown in Figure 2.1, is an infinite periodic discrete chain of two different springs and masses. Unit cell is defined as the periodically repeating segment of the diatomic chain. For the n^{th} unit cell, the equations of motion for the two neighboring masses can be given by [1, 34]

$$\begin{aligned}(-\omega^2 m_1 + k_1 + k_2)u_{2n} - k_1(u_{2n-1} + u_{2n+1}) = 0,\\ (-\omega^2 m_2 + k_1 + k_2)u_{2n+1} - k_2(u_{2n} + u_{2n+2}) = 0,\end{aligned} \tag{2.1}$$

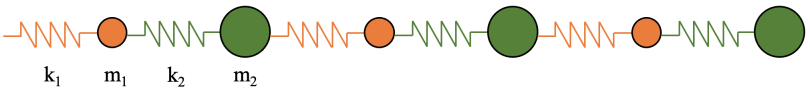

(a)

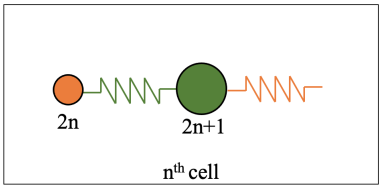

(b)

Figure 2.1: (a) An infinite 1-D diatomic chain and (b) n^{th} unit cell of the diatomic chain

where ω is the frequency and u is the displacement. Equation 2.1 for a plane wave can be further written in matrix form as

$$[\mathbf{K}(\gamma) - \omega^2\mathbf{M}]\mathbf{u}(\gamma)e^{in\gamma} = 0, \tag{2.2}$$

in which $\gamma = \mathbf{k}L$ and $\mathbf{u}(\gamma)e^{in\gamma}$ is the spatial part of the solution as defined by Floquet-Bloch theorem, which is commonly used to explore wave propagation in periodic structures [5, 34]. Here, L is the total length of the unit cell and $\mathbf{k}$ is the wavevector. The stiffness matrix, $\mathbf{K}$ and mass matrix, $\mathbf{M}$ can be written as

$$\mathbf{K}(\gamma) = \begin{bmatrix} k_1 + k_2 & -k_1e^{-i\gamma} - k_2 \\ -k_1e^{i\gamma} - k_2 & k_1 + k_2 \end{bmatrix}, \tag{2.3}$$

$$\mathbf{M} = \begin{bmatrix} m_1 & 0 \\ 0 & m_2 \end{bmatrix}. \tag{2.4}$$

For this two-degree-of-freedom (2-DOF) system, the eigenvalues can be found by solving for the roots of the characteristic equation which can be derived by setting the determinant of the coefficient matrix in Equation 2.2 equal to zero as shown in Equation 2.5. Dispersion curves for this simplified structure can then be created by plotting the two re-

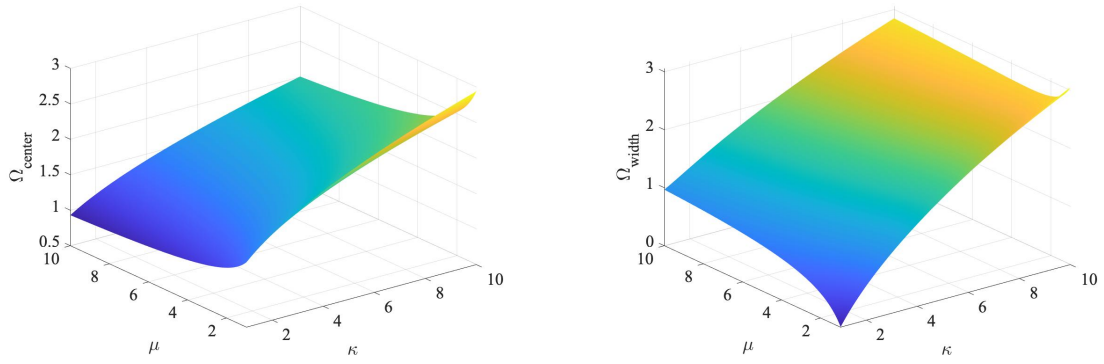

(a) (b)

Figure 2.2: (a) Bandgap center frequency and (b) width variation in diatomic chain model

sultant eigenvalues against $\mathbf{k}$.

$$\det(\mathbf{K}(\gamma) - \omega^2\mathbf{M}) = 0 \tag{2.5}$$

The local minimum of the larger eigenvalue defines the upper bound of the bandgap, whereas the local maximum of the smaller eigenvalue defines the lower bound of the bandgap. The bandgap width and center frequency variations with respect to mass and stiffness ratio in the unit cell are shown in Figure 2.2. Mass ratio, μ is defined as m_2/m_1 and stiffness ratio, κ is defined as k_2/k_1. Here, Ω (normalized by $\sqrt{k_1/m_1}$) is the non-dimensionalized frequency. It can be observed that when both mass and stiffness ratio are 1, the bandgap width is 0 which indicates that the diatomic chain is homogeneous. An ideal bandgap would be wider and occur at a lower center frequency. It can be noticed that increasing both mass and stiffness ratio results in a wider bandgap, and increasing stiffness ratio widens the bandgap much more substantially than increasing mass ratio. It can also be seen that increasing mass ratio lowers the bandgap center frequency while larger stiffness ratio results in higher bandgap center frequencies.

2.2 Dispersion Analysis Using the Transfer Matrix Method

While section 2.1 provides a fundamental understanding of bandgap formation in a diatomic structure, it is important to develop robust models which can capture bandgap formation in continuous systems such as periodic structures under axial, torsional, and bending vibrations. The eigenvalue problem for dispersion analysis is defined here using transfer matrix method (TMM) which relates the displacements and forces at the left and right unit cell boundaries. Figure 2.3 describes the periodic hydrogel structure of interest. The unit cell here is defined as the combination of non-swollen (segment a) and swollen (segment b) portions of an infinite periodic hydrogel structure. The transition between segment a and b is assumed to be sharp or step-like. Based on the trends noticed in the experiments, this model assumes that the mass density, ρ = 1023 kg/m^3 and Poisson's ratio, ν = 0.49 remain constant across the unit cell. The hydrogel is assumed to be a linear elastic material undergoing small deformations.

Table 2.1: Young's modulus, diameter, and length of the unit cell segments

Segment	E (kPa)	d (mm)	L (mm)
a	8.55	3.74	5.47
b	6.90	5.81	7.43

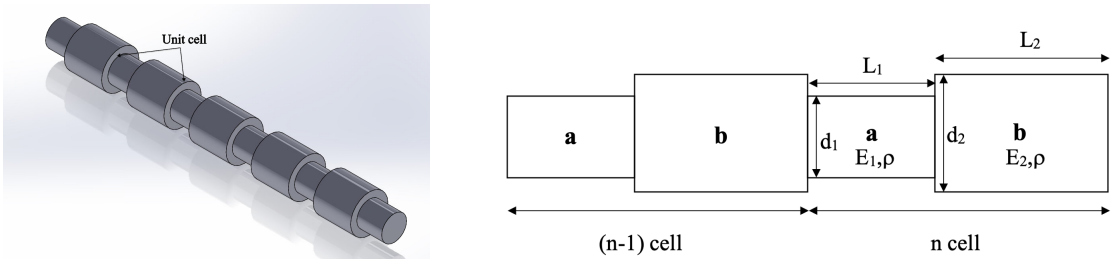

(a) (b)

Figure 2.3: (a) A finite periodic hydrogel structure with 5 unit cells (b) A schematic of the n^{th} and $(n-1)^{th}$ unit cells of an infinite periodic structure.

Dimensional and material specifications shown in Table 2.1 correspond to one of the hydrogel samples used in experiments and are used in this section to demonstrate the bandgap

formation for axial, torsional, and bending modes. Young's moduli of the hydrogel segments are obtained from tensile test.

2.2.1 Periodic Structures Under Bending Vibrations

A special emphasis is provided to the bending/transverse vibration model because the experimental results shown in chapter 4 focus on hydrogel structures under bending/transverse excitations. Bandgap formation in periodic structures under bending vibrations is modelled using two very common beam theories: Euler-Bernoulli and Timoshenko. While the Euler-Bernoulli theory can accurately model beams with high aspect ratios and provides a simple representation of the dynamics involved, the Timoshenko beam theory is ideal for structures where shear deformation and rotational inertia effects cannot be easily neglected. The equation of motion for an Euler-Bernoulli beam in the absence of damping and external load can be written as

$$EI\frac{\partial^4 w(x,t)}{\partial x^4} + \rho A\frac{\partial^2 w(x,t)}{\partial t^2} = 0 \tag{2.6}$$

where $w(x,t)$ is the transverse displacement of the periodic structure described in Figure 2.3, A is the cross-sectional area and I is the second moment of area [35]. For circular cross-section, I can be defined as

$$I = \frac{\pi}{64}d^4 \tag{2.7}$$

where d is the cross-sectional diameter. The solution to Equation 2.6 can then be given by

$$w(x,t) = e^{i\omega t}(W_1 e^{-i\mathbf{k}x} + W_2^N e^{-\mathbf{k}x} + W_3^N e^{i\mathbf{k}x} + W_4 e^{\mathbf{k}x}) \tag{2.8}$$

in which superscript, N denotes the near field component of the solution and wavenumber,

$\mathbf{k}$ is defined as

$$\mathbf{k} = \sqrt[4]{\frac{\rho A \omega^2}{EI}}. \tag{2.9}$$

The transfer matrix method relates the displacement and forces at the unit cell boundaries. In the case of bending vibrations, transverse displacement, slope, bending moment, and shear force continuities are considered at the boundaries of the unit cell shown in Figure 2.3 [36]. Slope, bending moment, and shear force are defined as

$$\theta = w'(x,t), \qquad M = EIw''(x,t), \qquad S = EIw'''(x,t) \tag{2.10}$$

respectively. The continuities of displacements and forces at the interface of the $(n-1)^{th}$ and n^{th} unit cell $(x = nL, L = L_1 + L_2)$ give

$$\begin{aligned} w_{n,a}(0) &= w_{n-1,b}(L), \\ w'_{n,a}(0) &= w'_{n-1,b}(L), \\ E_a I_a w''_{n,a}(0) &= E_b I_b w''_{n-1,b}(L), \\ E_a I_a w'''_{n,a}(0) &= E_b I_b w'''_{n-1,b}(L). \end{aligned} \tag{2.11}$$

Equation 2.11 can be written in matrix form as $\mathbf{AW}_{n,a} = \mathbf{BW}_{n-1,b}$ where, $\mathbf{W} = [W_1\ W_2\ W_3\ W_4]^T$. Similarly, the continuities at the interface of segments A and B of the n^{th} cell $(x = nL + L_1)$ yield

$$\begin{aligned} w_{n,a}(L_1) &= w_{n,b}(L_1), \\ w'_{n,a}(L_1) &= w'_{n,b}(L_1), \\ E_a I_a w''_{n,a}(L_1) &= E_b I_b w''_{n,b}(L_1), \\ E_a I_a w'''_{n,a}(L_1) &= E_b I_b w'''_{n,b}(L_1). \end{aligned} \tag{2.12}$$

which can then be written in matrix form as $\mathbf{CW}_{n,a} = \mathbf{DW}_{n,b}$. The two continuities

defined in matrix form establish the relationship between $n-1^{th}$ and n^{th} unit cell as

$$\begin{aligned} \mathbf{W}_{n,b} &= \mathbf{T}\mathbf{W}_{n-1,b}, \\ \mathbf{T} &= \mathbf{D^{-1}C A^{-1}B}, \end{aligned} \tag{2.13}$$

and $\mathbf{T}$ here is the transfer matrix of the system. Due to the periodic nature of the structure, $\mathbf{W_n}$ also needs to satisfy the Floquet-Bloch Theorem [5]. To re-iterate in matrix form, this theorem states

$$\mathbf{W}_n = e^{i\gamma}\mathbf{W}_{n-1}. \tag{2.14}$$

The dispersion curve plot can then be created by solving for the roots of the characteristic equation provided below

$$|\mathbf{T} - e^{i\gamma}\mathbf{I}| = 0 \tag{2.15}$$

where $\mathbf{I}$ is a 4 x 4 identity matrix. The roots of the characteristic equation provide wavevector, k for a given frequency, ω.

The Euler-Bernoulli beam model can overestimate bandgap width and location if the shear deformation and rotational inertia effects are not insignificant. The stimuli-responsive hydrogels used in this research have very low Young's modulus when compared to metals, plastics, and even rubber. The gel-based unit cells are also of low aspect ratio. Both of these factors can result in significant shear deformation and rotational inertia effects. In the absence of damping and external load, the equation of motion for a Timoshenko beam can be written as

$$EI\frac{\partial^4 w(x,t)}{\partial x^4} + \rho A\frac{\partial^2 w(x,t)}{\partial t^2} - \left(\rho I + \frac{EI\rho}{k_s G}\right)\frac{\partial^4 w(x,t)}{\partial x^2 \partial t^2} + \left(\frac{\rho^2 I}{k_s G}\right)\frac{\partial^4 w(x,t)}{\partial t^4} = 0 \tag{2.16}$$

where G is the shear modulus and β is the shear factor and it depends on the cross-section of the structure [37]. For a linear elastic material, G is given by

$$G = \frac{E}{2(1+\nu)}. \tag{2.17}$$

For a circular cross-section, the shear factor is defined as [38]

$$k_s = \frac{6(1+\nu)}{7+6\nu}. \tag{2.18}$$

The general harmonic solution for a Timoshenko beam can then be written as

$$w(x,t) = e^{i\omega t}(W_1 e^{\mathbf{k}_1 x} + W_2 e^{\mathbf{k}_2 x} + W_3 e^{\mathbf{k}_3 x} + W_4 e^{\mathbf{k}_4 x}) \tag{2.19}$$

in which $\mathbf{k}_{i=1:4}$ are the roots of

$$\mathbf{k}^4 + \left[\left(\frac{\rho I}{EI}\right)\omega^2 + \left(\frac{\rho}{k_s G}\right)\omega^2\right]\mathbf{k}^2 + \left(\frac{\rho A}{EI}\right)\omega^2\left[\left(\frac{\rho I}{k_s G A}\right)\omega^2 - 1\right] = 0. \tag{2.20}$$

Transfer matrix derivation and unit cell based boundary conditions similar to Euler-Bernoulli beam model are again utilized here to solve for the characteristic equation roots and ultimately create the dispersion curve plots [37]. Figure 2.4 compares the resultant dispersion curves from the Euler-Bernoulli and Timoshenko beam models for the periodic hydrogel structure with dimensions and material properties provided in Table 2.1. It can be observed that the Euler-Bernoulli beam model significantly overestimates the location and width of the first two bandgaps when compared to Timoshenko beam model.

2.2.2 Periodic Structures Under Axial and Torsional Vibrations

Axial and torsional models are not validated through experiments in this work, however these models are a good academic practice and can still prove to be useful if coupled

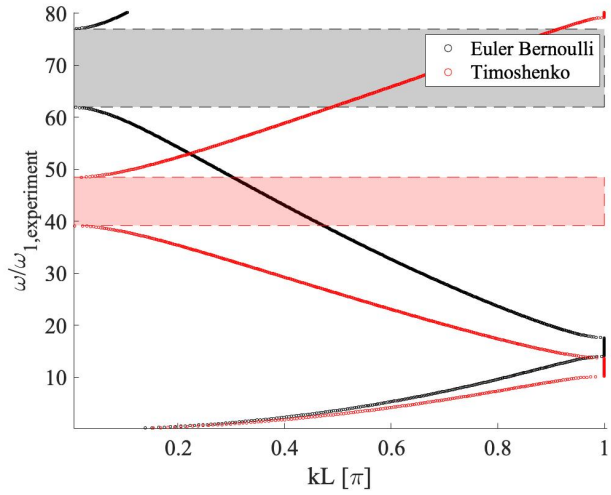

Figure 2.4: Dispersion curves created using Euler-Bernoulli and Timoshenko beam models for a periodic hydrogel structure. The horizontal shaded patches denote the relatively wider second bandgap in the respective models. Frequency axis here is normalized by the first experimental resonant frequency of a clamp-free periodic hydrogel beam under transverse base excitation.

modes of vibrations are to be considered for hydrogel structures. For structures under pure axial vibrations, the equation of motion in absence of damping and external forcing can be written as

$$EA\frac{\partial^2 u(x,t)}{\partial x^2} - \rho A\frac{\partial^2 u(x,t)}{\partial t^2} = 0, \tag{2.21}$$

where $u(x,t)$ is the axial displacement [35]. The general harmonic solution of the axial bar model is given by,

$$u(x,t) = e^{i\omega t}(U_1 e^{-i\mathbf{k}x} + U_2 e^{i\mathbf{k}x}), \tag{2.22}$$

where $\mathbf{k}$ is defined as

$$\mathbf{k} = \sqrt{\frac{\rho\omega^2}{E}}. \tag{2.23}$$

A TMM approach identical to the one discussed earlier in this section is again utilized to create the dispersion curve plots, however the axial continuities at the unit cell boundaries do not involve any out of plane rotation or shear deformation. The only displacement in

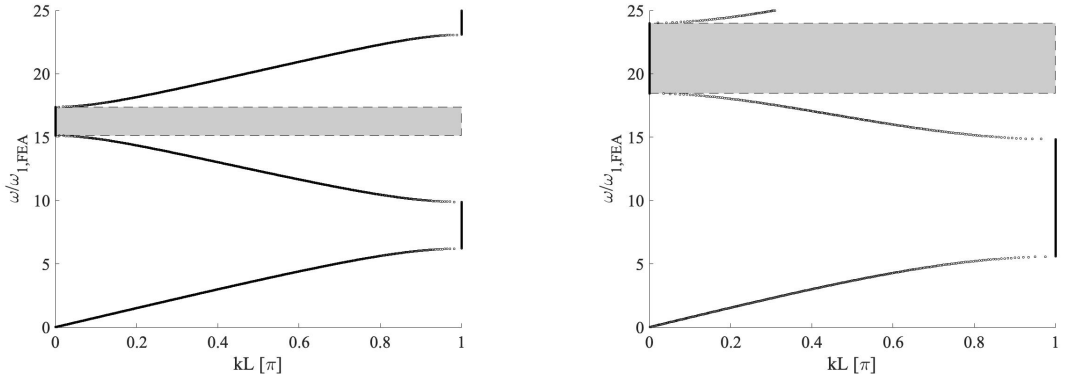

(a) (b)

Figure 2.5: Dispersion curves for a periodic hydrogel structure under (a) pure axial and (b) torsional vibrations. In absence of any experimental results, the frequency axes here are normalized by the first resonant frequency as predicted by the respective finite element models which are discussed in detail in chapter 3.

question is $u(x,t)$, whereas the axial force, F is the only force and can be defined as

$$F = EAu'(x,t). \tag{2.24}$$

In order to re-derive the transfer matrix and the roots of the characteristic equation, $u(x,t)$ and F can be further evaluated at the two interfaces of interest in our unit cell as shown in Equation 2.10 and 2.11. Periodic structures (with circular cross-section) under pure torsional vibrations can be modelled using the same approach as the axial model but $u(x,t)$ is replaced by angular displacement, $\theta(x,t)$. Additionally, Young's modulus, E and cross-sectional area, A would be replaced by their rotational counterparts, shear modulus, G and polar moment of inertia, J respectively. A sample dispersion curve plot is provided for both axial and torsional models in Figure 2.5. Both axial and torsional models utilize the dimensional and material specifications provided in Table 2.1.

2.3 Case Studies

An ideal bandgap is wide and occurs at a desired frequency, which is often a relatively low frequency in vibration applications. It is essential to identify the parameters in the system which can help idealize the bandgap. In the case of periodic structures, varying the extent of material and geometric periodicity in the unit cell can help with bandgap tuning. Diameter ratio, δ, Young's modulus ratio, ϵ, and length ratio, α of the unit cell are defined as

$$\delta = \frac{d_b}{d_a}, \qquad \epsilon = \frac{E_a}{E_b}, \qquad \alpha = \frac{L_b}{L_a}. \tag{2.25}$$

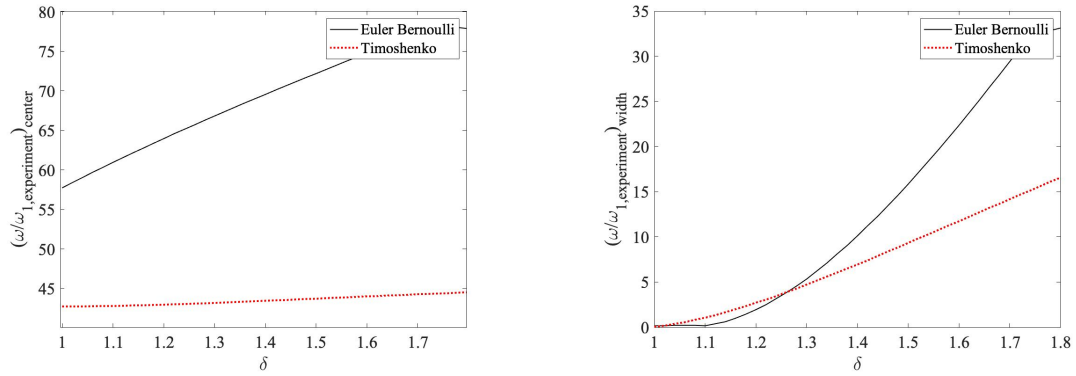

(a) (b)

Figure 2.6: Second bandgap (a) center frequency and (b) width variation in Euler-Bernoulli and Timoshenko beam models versus diameter ratio, δ

Each of these parameters are independently varied over a range of 1-1.8 while others are held constant at 1. Additionally, unit cell length ratio is varied while the total length of unit cell remains constant, thus altering the length proportions of the swollen and non-swollen segments within the unit cell. UV irradiation in hydrogels increases the diameter but decreases Young's modulus of the swollen segment which explains the reversed definition of ϵ in Equation 2.25. All the parametric sweeps use the initial parameters of the

non-swollen segment provided in Table 2.1. It is important to note that unit cell length ratio variation in absence of any diameter or material periodicity will simply not yield any bandgaps, hence swollen segment diameter and Young's modulus provided in Table 2.1 are also used for unit cell length ratio sweep. The parametric sweep results shown here solely focus on the second bandgap of the Euler-Bernoulli and Timoshenko beam models due to their relevance to the experimental efforts which are made to validate the second bandgap formation in periodic structures under transverse excitation.

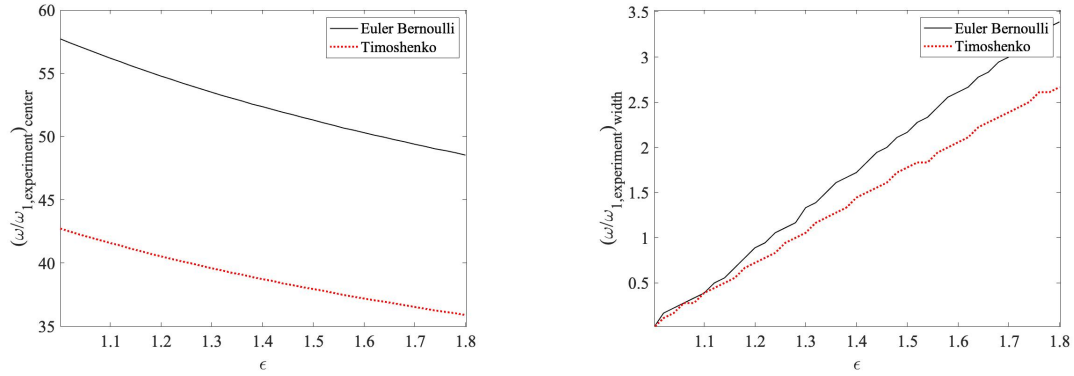

(a) (b)

Figure 2.7: Second bandgap (a) center frequency and (b) width variation in Euler-Bernoulli and Timoshenko beam models versus Young's modulus ratio, ϵ

It can be observed in Figure 2.6 that increasing δ tends to increase the width of the bandgap but it also results in higher center frequencies for both Euler-Bernoulli and Timoshenko beam models. It can be observed in Figure 2.7 that increasing ϵ widens the bandgap and reduces the center frequency, however the variations in bandgap width and center frequency are not as significant when compared to diameter ratio sweep. Additionally, it can be observed in Figure 2.8 that increase in α marginally increases the center frequency while reducing the width in Euler-Bernoulli and Timoshenko beam models.

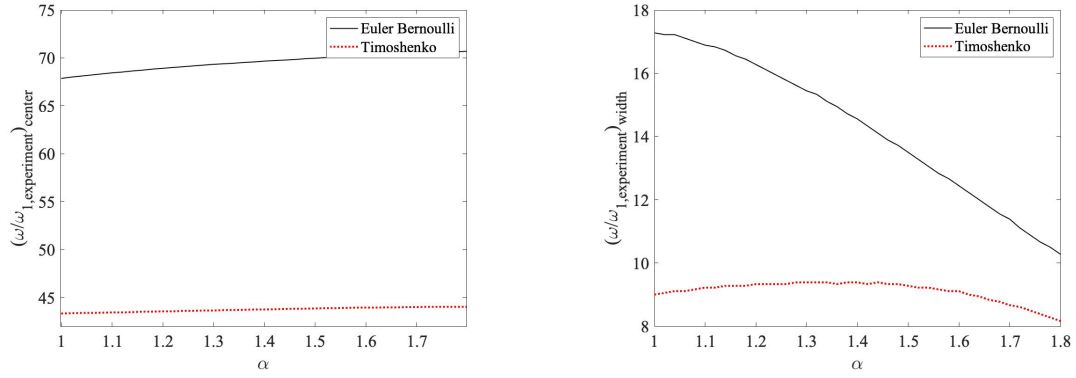

(a) (b)

Figure 2.8: Second bandgap (a) center frequency and (b) width variation in Euler-Bernoulli and Timoshenko beam models versus unit cell length ratio, α

2.4 Summary and Conclusions

This chapter focuses on the development of dispersion analysis to study bandgap formation and tuning in periodic hydrogel structure. Bandgap formation in an infinite diatomic chain, which is the simplest representation of periodic structures, is first analyzed to demonstrate how change in mass and stiffness ratios can change the width and center frequency of the bandgaps. Transfer matrix method is then employed to derive the eigenvalue problem for a unit cell of a continuous infinite periodic structure, which is further solved to create dispersion curve plots. Both Euler-Bernoulli and Timoshenko beam theories are utilized to analyze bandgap formation in periodic structures under bending vibrations. While Euler-Bernoulli beam model can provide a simpler representation of dynamics involved, Timoshenko beam model considers shear deformation and rotational inertia effects which is non-negligible in soft hydrogel structures. It can noticed that in the presence of shear deformation and rotational inertia effects, Euler-Bernoulli beam model consistently overestimates bandgap width and location. Numerous case studies discussed in this chapter reveal that it is possible to tune bandgaps upon variations in parameters such as diameter, Young's modulus, and unit cell length ratio.

CHAPTER 3
FINITE STRUCTURE FREQUENCY RESPONSE ANALYSIS USING FINITE ELEMENT METHOD

This chapter discusses the finite element method (FEM) based frequency response analysis to study bandgaps in periodic hydrogel structures. FEM is an alternative to dispersion analysis discussed in chapter 2 but it provides insight into how these bandgaps appear in a periodic structure with a finite number of unit cells. Additionally, frequency response analysis results discussed here directly relate to the shaker vibration experiments which use hydrogel structures with 7 unit cells. FEM spatially discretizes a given structure into smaller elements for which the mass and stiffness matrices can be derived using Hamilton's principle. The local element matrices can then be combined together using transformation matrices to define the multi-degree-of-freedom (M-DOF) vibration problem. The mass and stiffness matrix derivation is discussed here for clamp-free Euler-Bernoulli and Timoshenko beams under transverse base excitation. Finite periodic structures under pure axial and torsional vibrations are also briefly discussed in this chapter. An infinite periodic structure will entirely prohibit wave propagation in the bandgap region, however structures with a finite number of unit cells can only attenuate the vibrations to some extent. The quality of attenuation would depend on parameters such as number of unit cells and extent of material and geometric periodicity. The effect of these parameters on the bandgap formation in Euler-Bernoulli and Timoshenko periodic beam structures is further studied in this chapter.

3.1 FEM Based Formulations for Periodic Structures Under Bending Vibrations

Both the Euler-Bernoulli and Timoshenko beam theories are again utilized here to analyze the periodic structures under bending/transverse vibrations. For both beam theories, the local element based mass, stiffness matrices and forcing vector derivation along with

the global matrix transformation is discussed in this section. Modal superposition method is further used with these global matrices to create the frequency response of a cantilever periodic beam.

3.1.1 Mass and Stiffness Matrix Derivation- Euler-Bernoulli Beam

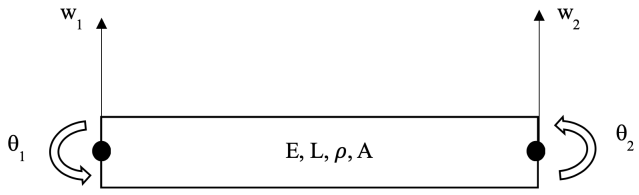

Figure 3.1: A 2 node Euler-Bernoulli beam element.

For an elastic body, the generalized Hamilton's Principle is

$$\mathbf{T} = \int_{t_1}^{t_2} [\delta(T - U + W_{nc})]dt, \tag{3.1}$$

where the total kinetic energy (T), the total potential energy (U) are defined as

$$T = \frac{1}{2}\int_0^L \rho A \dot{w}(x,t)^2 dx, \qquad U = \frac{1}{2}\int_0^L EI w_{xx}(x,t)^2 dx \tag{3.2}$$

for a single free-vibration Euler-Bernoulli beam element with a constant cross-sectional area, A as shown in Figure 3.1 [35]. The total non-conservative work, W_{nc} is assumed to be 0. Here, $w(x,t)$ is the total transverse displacement of the beam element. Dot superscripts in Equation 3.1.1 denote time base derivative whereas subscripts, xx denote second partial derivative with respect to x. Modal damping is used to model the loss in the system and is considered later in modal superposition process. Each node in the beam element has two degrees of freedom: transverse displacement, $w(x,t)$ and nodal rotation, $w_x(x,t)$ (θ_w). The spatial component of $w(x,t)$ can be written in a cubic polynomial form

$$w(x) = a_0 + a_1\, x + a_2\, x^2 + a_3\, x^3. \tag{3.3}$$

Equation 3.3 can be re-written in matrix form as

$$w(x) = \mathbf{X}\mathbf{a}, \tag{3.4}$$

where polynomial vector, $\mathbf{X} = \begin{bmatrix} 1 & x & x^2 & x^3 \end{bmatrix}$ and coefficient vector, $\mathbf{a}^t = \begin{bmatrix} a_0 & a_1 & a_2 & a_3 \end{bmatrix}$. $w(x)$ can also be written as

$$w(x) = \mathbf{N}\psi, \tag{3.5}$$

where $\mathbf{N}$ is the shape function vector and ψ is the generalized nodal coordinate vector which is defined as

$$\psi^t = \begin{bmatrix} w_1 & \theta_1 & w_2 & \theta_2 \end{bmatrix}, \tag{3.6}$$

and it can also be found by evaluating Equation 3.3 and its first derivative with respect to x at $x = 0$ and L. This relationship can be written as

$$\psi = \mathbf{B}\mathbf{a}. \tag{3.7}$$

Substituting the definition of $\mathbf{a}$ from Equation 3.7 into Equation 3.4 yields,

$$\mathbf{N} = \mathbf{X}(x)\mathbf{B}^{-1}. \tag{3.8}$$

Equation 3.5 can be substituted back into Equation 3.1.1 to extract the mass and stiffness matrix for an Euler-Bernoulli beam element which can be expressed as

$$\mathbf{m_e} = \int_0^L \rho A \dot{\psi}^t \mathbf{N}^t \mathbf{N} \dot{\psi} dx, \qquad \mathbf{k_e} = \int_0^L EI \psi_{xx}^t \mathbf{N}_{xx}^t \mathbf{N}_{xx} \psi_{xx} dx. \tag{3.9}$$

If the forcing mechanism for the structure is the motion of the clamped end in the transverse direction, the effective force on the structure is a result of the translational inertia

in that direction and it contributes to the total kinetic energy term in Equation 3.1. In this case, the element force vector is given by

$$\mathbf{f}_e = \int_0^L -\rho A a_b \mathbf{N}^T dx \tag{3.10}$$

where a_b is the base acceleration [39, 40].

3.1.2 Mass and Stiffness Matrix Derivation- Timoshenko Beam Element

Several FEM based approaches have been studied and can be used to derive the mass and stiffness matrices of a single Timoshenko beam element. Unlike Euler-Bernoulli beam element, the rotation of the neutral axis in Timoshenko beam is a combination of the transverse displacement related rotation, and shear deflection angle, θ_s. The element stiffness matrix is derived using the force and moment relations of the Timoshenko beam element under static equilibrium, whereas the element mass matrix is derived using the elemental kinetic energy term (similar to Euler-Bernoulli beam element derivations) [41]. Using the static equilibrium approach, the stiffness matrix for a Timoshenko beam element is defined as

$$\mathbf{k}_e = \frac{EI}{(1+\eta)L^3} \begin{bmatrix} 12 & 6L & -12 & 6L \\ & (4+\eta)L^2 & -6L & (2-\eta)L^2 \\ & & 12 & -6L \\ Symmetric & & & (4+\eta)L^2 \end{bmatrix}, \tag{3.11}$$

where $\eta = 12EI/Gk_sAL^2$ and k_s is the shear factor. The kinetic energy of a Timoshenko beam can be given by

$$T = \frac{1}{2}\int_0^L \rho A \dot{w}(x,t)^2 dx + \frac{1}{2}\int_0^L \rho I(\dot{\theta}_w(x,t) + \dot{\theta}_s(x,t))^2 dx, \tag{3.12}$$

where θ_w is the rotation angle which is a result of the transverse displacement [41, 42]. The

kinetic energy term helps with the derivation of the element mass matrix which can then be written as

$$M = \frac{\rho A L}{210(1+\eta)^2} \tag{3.13}$$

$$N = \begin{bmatrix} 70\eta^2+147\eta+78 & (35\eta^2+77\eta+44)\frac{L}{4} & 35\eta^2+63\eta+27 & -(35\eta^2+63\eta+26)\frac{L}{4} \\ & (7\eta^2+14\eta+8)\frac{L^2}{4} & (35\eta^2+63\eta+26)\frac{L}{4} & -(7\eta^2+14\eta+6)\frac{L^2}{4} \\ & & 70\eta^2+147\eta+78 & -(35\eta^2+77\eta+44)\frac{L}{4} \\ Symmetric & & & (7\eta^2+14\eta+8)\frac{L^2}{4} \end{bmatrix}$$

$$\mathbf{m}_{e,\rho A} = M * N \tag{3.14}$$

$$M_I = \frac{\rho I}{30(1+\eta)^2 L} \tag{3.15}$$

$$\mathbf{m}_{e,\rho I} = M_I \begin{bmatrix} 36 & -(15\eta-3)L & -36 & -(15\eta-3)L \\ & (10\eta^2+5\eta+4)L^2 & (15\eta-3)L & (5\eta^2-5\eta-1)L^2 \\ & & 36 & (15\eta-3)L \\ Symmetric & & & (10\eta^2+5\eta+4)L^2 \end{bmatrix} \tag{3.16}$$

$$\mathbf{m}_e = \mathbf{m}_{e,\rho A} + \mathbf{m}_{e,\rho I} \tag{3.17}$$

The same forcing term as Euler-Bernoulli beam element is used again with the Timoshenko beam element to evaluate the structural response with respect to base excitation.

3.1.3 Tranformation Matrices

Transformation matrices are then used to convert the local element matrices into the global ones. These transformation matrices are of the size, 4 x n-DOF (total degrees of freedom in the structure) and they are designed to populate the global matrix along the diagonal. Global mass and stiffness matrices, $\mathbf{M}$ and $\mathbf{K}$ along with global forcing vector, $\mathbf{F}$ are defined as

$$\mathbf{M} = \sum_{i=1}^{n} \mathbf{T}_i^T \mathbf{m}_i \mathbf{T}_i, \qquad \mathbf{K} = \sum_{i=1}^{n} \mathbf{T}_i^T \mathbf{k}_i \mathbf{T}_i, \qquad \mathbf{F} = \sum_{i=1}^{n} \mathbf{T}_i^T \mathbf{f}_i \tag{3.18}$$

where n is the total number of elements in the structure and $\mathbf{T}_i$ is the transformation matrix for the i^{th} element. The global equation of motion is then given by

$$\mathbf{M}\ddot{\psi} + \mathbf{C}\dot{\psi} + \mathbf{K}\psi = \mathbf{F}, \tag{3.19}$$

where $\mathbf{C}$ is the global damping matrix. Necessary changes can be made to the global matrices to consider the boundary conditions of a given structure. For instance, a clamp free boundary condition for an Euler-Bernoulli beam can be accounted in Equation 3.12 by truncating the first two rows and columns of the matrices which would indicate that the first nodal coordinate is fixed. In Timoshenko beams, the rotation at the clamped end is not necessarily zero due to the presence of shear deformation so only the first row and column is truncated from the global matrices. These truncated matrices can then be used to setup the eigenvalue problem which can yield the natural frequencies and mode shapes for the structure.

3.1.4 Modal Superposition

Modal superposition method utilizes the resultant natural frequencies and mode shapes to create the vibrational response for a given set of forcing vector. Just like the name suggests, modal superposition adds the response for each mode shape for a certain input excitation frequency. Using modal coordinates, Equation 3.12 is decoupled into n-DOF number of single-degree-of-freedom equations (S-DOF) and a modal damping ratio, ζ_r = 0.01 is applied to all modes of vibrations. The generalized variable per base acceleration, $\beta(\omega)$ can be given by

$$\beta(\omega) = \sum_{r=1}^{nDOF} \frac{\phi_r \phi_r^T \mathbf{F}^*}{\omega_r^2 - \omega^2 + 2i\zeta_r \omega \omega_r}, \tag{3.20}$$

where $\mathbf{F}^* = \mathbf{F}/a_b$ (base excitation), ϕ_r is the r^{th} mass normalized mode, ω_r is the r^{th} natural frequency of the structure, ζ_r is the r^{th} modal damping ratio and ω is the excitation frequency. It is important to note that in the case of base excitation, the transverse displacement and slopes are both relative to the base motion. Therefore, the absolute response function per base displacement or transmissibility, $\beta_{abs}(\omega)$ can be defined as

$$\beta_{abs}(\omega) = 1 - \omega^2 \beta(\omega). \tag{3.21}$$

A 7 unit cell and clamp-free hydrogel structure under base excitation with dimensions and material properties found in Table 2.1 is considered here to plot the transmissibility at the tip. As shown in Figure 3.2, Euler-Bernoulli FEM model overestimates the location and width of the bandgap when compared to Timoshenko FEM model which considers shear deformation and rotational inertia. It can also be noticed that the FEM results shown in Figure 3.2 agree well with the TMM results (chapter 2). The attention is again provided to the second bandgap here because the first bandgap is relatively narrow and does not provide significant response attenuation. Transmissibility heat maps are further generated as functions of ω and response location, x while the structure is excited at the base. It can be observed in Figure 3.3 that the attenuation within the bandgap region increases as x

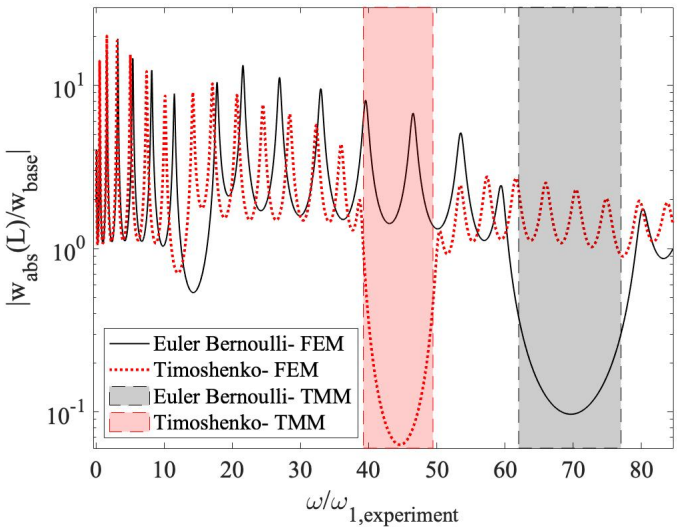

Figure 3.2: Transmissibility evaluated at the tip while the hydrogel structure with 7 unit cells is excited at the base. Both Euler-Bernoulli and Timoshenko FEM models have a modal damping, ζ_r = 0.01 for all vibration modes. The shaded patches denote the second bandgap as predicted by TMM approach.

moves towards the free end ($x/L = 1$).

3.2 FEM Based Formulations for Periodic Structures Under Axial and Torsional Vibrations

Formulations similar to Euler-Bernoulli and Timoshenko FEM models are again employed to derive the mass and stiffness matrices for hydrogel structures under pure axial or torsional vibrations. Hamilton's Principle (Equation 3.1) can be used again along with the total kinetic and potential energy terms to re-derive global equations of motion for FEM local elements under pure axial or torsional excitations. The total kinetic (T) and potential energy (U) for an element under going pure axial deformation can be defined as

$$T = \frac{1}{2}\int_0^L \rho A \dot{u}(x,t)^2 dx, \qquad U = \frac{1}{2}\int_0^L EA u_x(x,t)^2 dx \tag{3.22}$$

in which $u(x,t)$ represents the axial displacement in the structure. Unlike the Euler-Bernoulli beam element shown in Figure 3.1, an element under pure axial load would

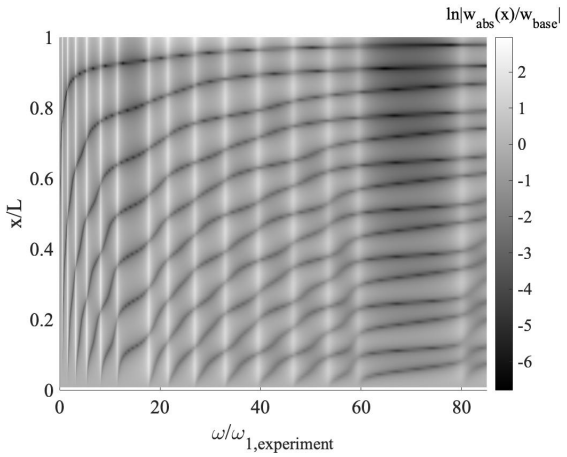

(a)

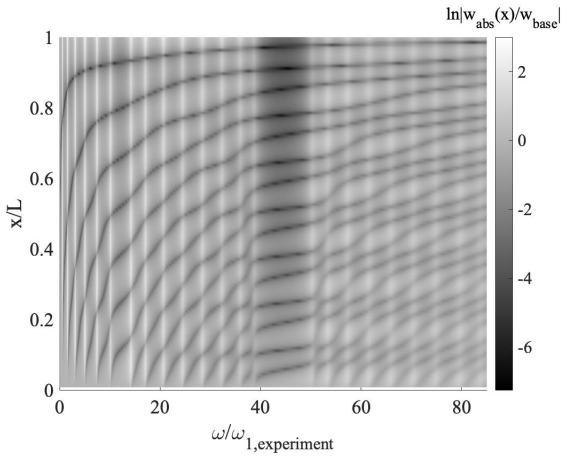

(b)

Figure 3.3: Transmissibility versus response location, x and excitation frequency, ω for a) Euler-Bernoulli and b) Timoshenko FEM models.

have a single degree of freedom at each node. The spatial component of $u(x,t)$ can then be written with a linear fit as

$$u(x) = a_0 + a_1\, x. \tag{3.23}$$

The shape function derivation process shown in subsection 3.1.1 (Equation 3.4-3.9) can then be used to create the shape functions for the axial element and ultimately, local mass and stiffness matrices [35]. An identical modal superposition approach (Equation 3.20) can also be used to model the axial transmissibility. Additionally, FEM model for a structure under pure angular loading can be created by using the rotational counterparts of the system

with axial FEM derivation (G and J in place of E and A respectively).

Tip transmissibility is then plotted by normalizing the tip response with response at the first free node next to the fixed end while a harmonic point force is applied to this node. $\mathbf{F}^*$ in Equation 3.13 now corresponds to a point force applied to a certain node in the discretized structure. It can be observed in Figure 3.4 that axial and torsional FEM models predict a much better response attenuation in the first bandgap compared to the second bandgap unlike the bending FEM models. Additionally, there is an excellent agreement between FEM bandgaps and TMM results from chapter 2.

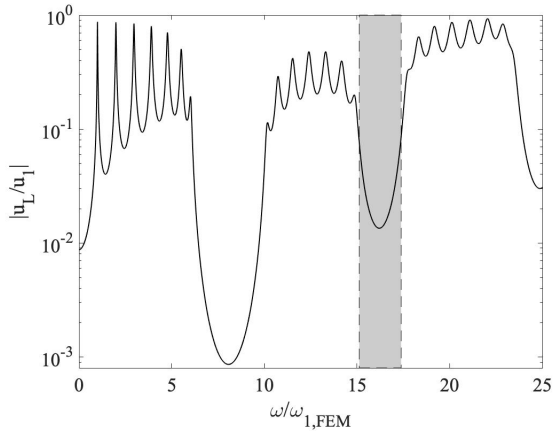

(a)

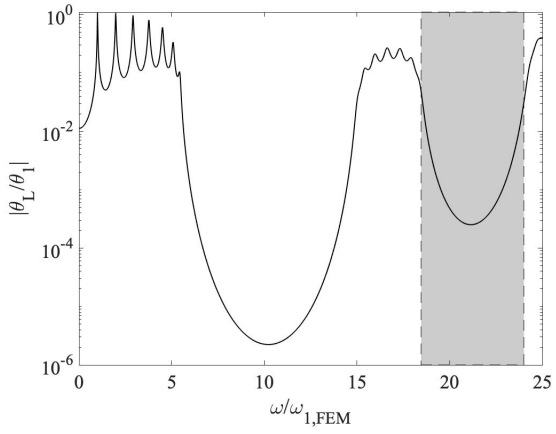

(b)

Figure 3.4: Transmissibility evaluated at the tip for (a) Axial and (b) Torsional FEM models while the hydrogel structure with 7 unit cells is excited at first free node next to the fixed end. Both FEM models have a modal damping, ζ_r = 0.01 for all axial and torsional modes.

3.3 Case Studies

Parametric sweeps discussed in section 2.3 are again performed with the Euler-Bernoulli and Timoshenko FEM models to examine how the bandgap features vary with respect to parameters such as number of unit cells, diameter, Young's modulus and unit cell length ratio as defined in Equation 2.25. Clamp free boundary conditions are considered for all the case studies and a constant modal damping ratio, ζ_r = 0.01 is used for all the vibration modes. While dispersion analysis case studies in chapter 2 already provide an understanding of how bandgap center frequency and width vary with parameters of interest, FEM model sweeps also study the variation in the response attenuation within the bandgap region. The results shown here also emphasize on the much wider second bandgap.

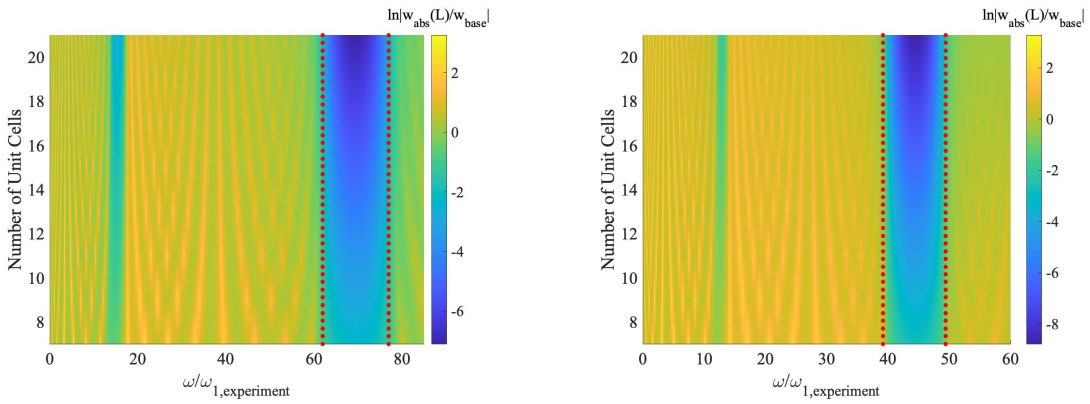

Figure 3.5: Tip transmissibility versus number of unit cells and excitation frequency, ω for (a) Euler-Bernoulli and (b) Timoshenko FEM models. Overlaid scatter plots (red) denote the second bandgap as predicted by TMM.

Figure 3.5 demonstrates how the attenuation increases within the bandgap as the number of unit cells increase. It is important to note that increasing the number of unit cells simply increases the total length of the structure without varying any unit cell parameters such as δ,ϵ, and α. With further increase in number of unit cells, it can be expected that the attenuation in the bandgap would also further increase because the structure slowly begins to approach an infinite periodic structure which entirely prohibits wave propagation within

bandgaps. If the bandgap occurs between m^{th} and $m+1^{th}$ resonant peaks, it can be noticed that m also increases with number of unit cells. Such behavior can be attributed to increase in overall length which is inversely proportional to resonant frequencies.

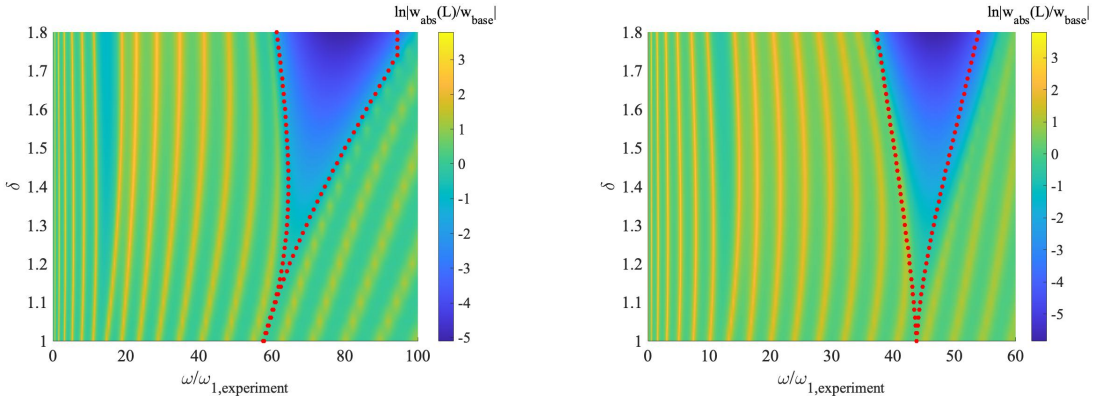

Figure 3.6: Tip transmissibility versus diameter ratio, δ and excitation frequency, ω for (a) Euler-Bernoulli and (b) Timoshenko FEM models.

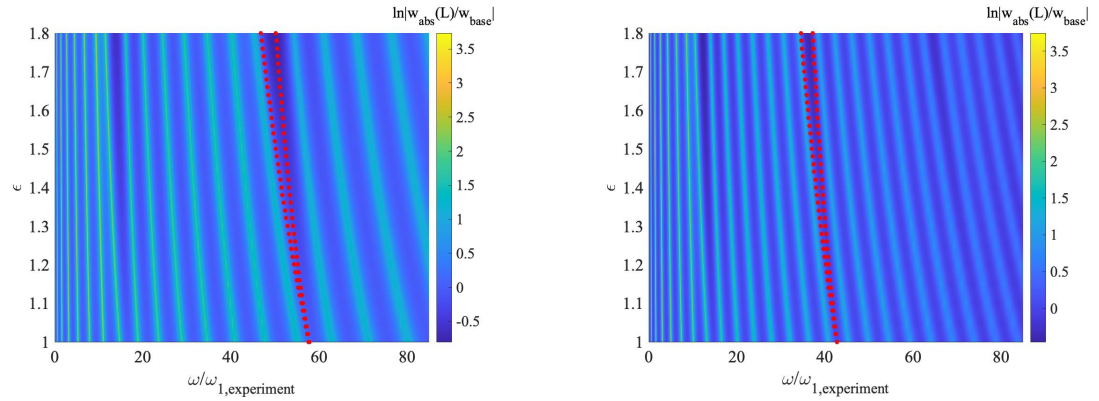

Figure 3.7: Tip transmissibility versus Young's modulus ratio, ϵ and excitation frequency, ω for (a) Euler-Bernoulli and (b) Timoshenko FEM models.

For diameter, Young's modulus, and unit cell length ratio sweeps, FEM models consider a structure with 7 unit cells (same as the samples used in the shaker based experiments discussed in chapter 4). An excellent agreement is again noticed between FEM and TMM results in Figure 3.6, 3.7 and 3.8. As shown in Figure 3.6, larger diameter ratios result in a much wider bandgap which also possesses better attenuation, however bandgap center fre-

quency increase can also be noticed. Figure 3.7 also concludes that larger Young's modulus ratios tend to widen the bandgaps while reducing the center frequencies, however bandgap attenuation and widths of the bandgaps are not as pronounced when compared to diameter ratio sweeps. Unit cell length ratio variations on the other hand, reduce the bandgap width and also marginally increase the center frequencies as shown in Figure 3.8.

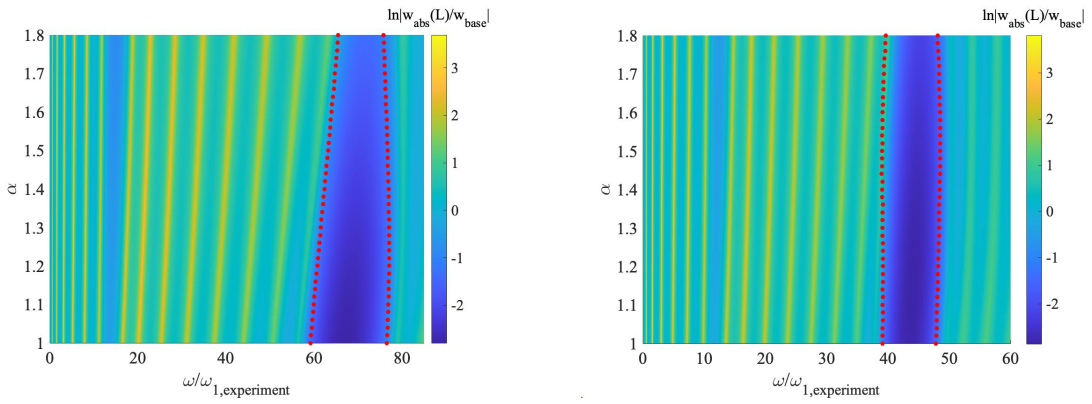

Figure 3.8: Tip transmissibility versus unit cell length ratio, α and excitation frequency, ω for (a) Euler-Bernoulli and (b) Timoshenko FEM models.

3.4 Summary and Conclusions

A finite element method model is utilized here for studying bandgap formation and tuning in finite periodic structures. While dispersion analysis, discussed in chapter 2, would be sufficient to predict the bandgap location and width, it is essential to create a model which can capture the response and bandgap appearance in a finite periodic structure under an external loading. It is observed that bandgap attenuation improves with increase in number of unit cells in the finite periodic structure. Additionally, it can be noticed that bandgap attenuation is largest at the free end of the cantilever configuration. Finite element model case studies also validate the dispersion analysis results from chapter 2 as very good agreement is found between the two approaches for all the models.

For the hydrogel structures studied in this research, diameter and Young's modulus ra-

tios are both an outcome of UV based activation, hence they are not entirely independent. However, it is not challenging to design periodic structures for either geometric or material periodicity. The study developed and discussed in chapter 2 and 3 can also be used to predict and tune bandgaps in periodic non-hydrogel structures. Based on the design requirements, one can tune any of these parameters to achieve the desired bandgap. Large diameter and Young's modulus ratios along with lower length ratios would certainly widen the bandgap. Without compromising the bandgap width, bandgap can shift to a lower center frequency with larger Young's modulus and smaller unit cell length ratios.

CHAPTER 4
EXPERIMENTAL BANDGAP FORMATION AND TUNING IN HYDROGEL-BASED PERIODIC CANTILEVER BEAM CONFIGURATIONS

This chapter discusses the experimental efforts to study bandgap formation in periodic hydrogel structures. Shaker vibration tests are performed on cantilever hydrogel configurations to measure the response at the free end while the structure is excited at the base with rectangular noise voltage signal. COMSOL model with additional factors such as gravitational body load is also considered to ensure good match with the experimental findings. The bandgap tuning with respect to leucohydroxide (TPMLH) concentration and unit cell length ratio, α is further studied. TPMLH concentration determines the swelling capacity of a hydrogel, hence it ultimately controls geometric and material periodicity in the structure. Unlike the case studies discussed in chapter 2 and 3, case studies here will focus on bandgap tuning with respect to the coupled effects of geometric and material periodicity. Finally, diatomic chain model discussed in chapter 2 is again used to qualitatively analyze the experimental trends.

4.1 Periodic Hydrogel Synthesis

The photo-responsive hydrogels are prepared using the conventional protocol for polyacrylamide-co-triphenlymethane leucohydroxide (commonly referred as leucohydroxide or TPMLH in this thesis) hydrogel [33]. The PAAm-co-TPMLH hydrogel is synthesized using 2-3 M (Moles) acrylamide (AAm), 10-20 mM N,N'-methylenebisacrylamide (Bis), and 30-50 mM TPMLH. An aluminum foil with evenly spaced cut outs (also referred as photomask) is used for localized photo-activation of homogeneous hydrogels. The photomask is placed between the hydrogel and a 365 nm UV light (LED, 40 mW/cm^2), the hydrogel is activated into a periodic configuration. As shown in Figure 4.1, the photo-

activated hydrogel is allowed to freely swell in de-ionized (DI) water for 4 hours to achieve its periodic state.

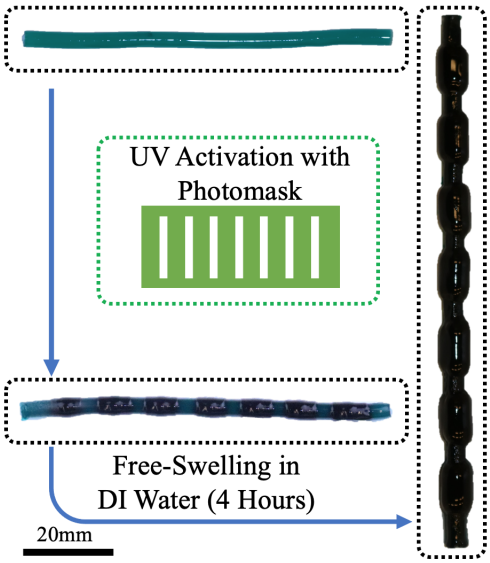

Figure 4.1: Homogeneous to periodic transition for TPMLH based hydrogels.

The Young's modulus for the swollen and non-swollen segment of the sample is extracted from tensile test upon the completion of shaker experiments discussed in this chapter. It is observed that the Young's modulus falls in the range of 4-12 kPa for all samples. The resultant softness in the structures makes them very fragile, hence the number of unit cells in the periodic samples is limited to 7. In chapter 2 and 3, the periodic structure is assumed to have a step-like transition between non-swollen and swollen segments. However, it can be noticed in Figure 4.1 that the periodic hydrogels have gradual transition zones between non-swollen and swollen segments. The transition zones represent both the geometric and material transition between the segments of a unit cell.

4.2 Shaker Test Setup

The shaker vibration tests are performed using a Brüel and Kjær Vibration Exciter Type 4809 which connects to the hydrogel sample via an acrylic clamp. As shown in Figure 4.2, a uni-axial PCB accelerometer is attached to the back end of the acrylic clamp

and signal conditioner (Kistler Type 5134) with a constant gain is used to improve the signal-to-noise ratio of the recorded base acceleration. Laser Doppler vibrometer (OFV 505) is used to measure the velocity at the tip of the hydrogel and a 20 kHz low pass filter is used to improve the signal-to-noise ratio. Data acquisition module, NI-9223 is used to record tip and base response. Low voltage rectangular noise signal with Hamming window is provided to the shaker using NI signal express. The voltage signal is sent to the shaker via power amplifier (LDS-PA25E) with a constant gain. The soft nature of hydrogels makes them susceptible to immediate fractures or fatigue failures if the structure is excited with high voltages/large displacement amplitudes, hence only linear experiments are performed on hydrogels (low voltages/ low displacement amplitudes).

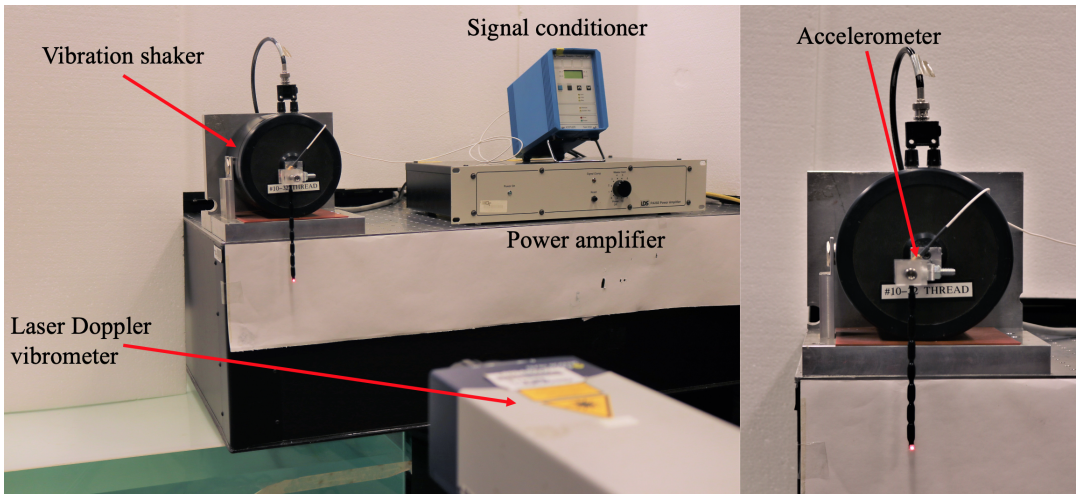

Figure 4.2: Shaker vibration test setup with the periodic hydrogel sample attached at the clamp.

The recorded time histories from accelerometer and OFV 505 are also averaged using NI signal express. The tip velocity measured by OFV 505 is normalized by the base acceleration and magnitude of tip transmissibility is then defined as

$$|\beta_L(\omega)| = \omega|\xi_L(\omega)|, \tag{4.1}$$

where $\beta_L(\omega)$ is the tip transmissibility, $\xi_L(\omega)$ is the tip velocity (absolute with respect to the moving base) normalized by base acceleration and ω is the excitation frequency. Figure 4.3

compares the tip transmissibility for homogeneous and periodic hydrogel structures. The bandgap formation can be clearly observed for the periodic structure (denoted by red patch in Figure 4.3). In this specific type of experiment, the bandgap can be physically interpreted as a band of frequency where the magnitude of tip displacement is less than base displacement.

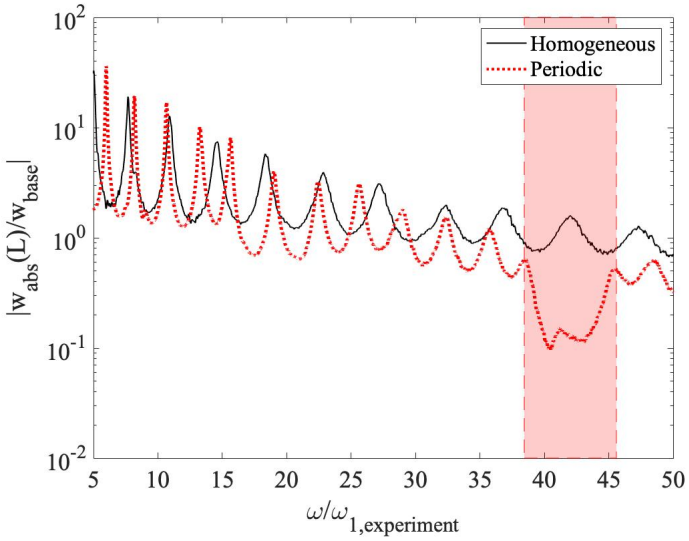

Figure 4.3: Tip transmissibility for homogeneous and periodic hydrogels while they are excited at the base. The shaded patch here denotes the region between the 15^{th} and 16^{th} resonance of the periodic structure.

4.3 FEM Model with Gravitational Body Load

Both chapter 2 and 3 focus entirely on the formulation and evaluation of Euler-Bernoulli and Timoshenko beam models in context with the periodic structures. It is concluded that Timoshenko beam model would prove to be a more accurate model as the shear deformation and rotational inertia in these soft hydrogel structures are non-negligible. This softness in hydrogels, however introduces additional geometric non-linearities which are considered in COMSOL FEM model. As shown in Figure 4.4, the clamped periodic hydrogel structure happens to have a static axial deflection under its own weight owing to a very low Young's modulus. It can also be observed that this deflection is not constant across the structure, i.e.

unit cells closer to the clamp have larger deflections when compared to unit cells closer to the free end. Such behavior can be attributed to the fact that weight/gravitational load is a volumetric force.

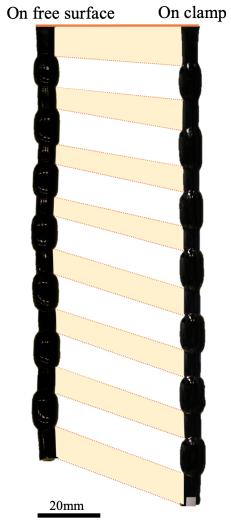

Figure 4.4: The axial deformation of the hydrogel while on clamp due to gravitational body load.

Having an uneven distribution of both axial stress and static deflection would make unit cells different from one another, hence jeopardizing the structural periodicity. COMSOL model uses the average dimensions of the hydrogel (measured while it sits on a free surface) along with built-in gravity body load to account for static axial deflection. Frequency response study is then employed onto a statically deformed structure. The static axial deflection is modeled to be a geometric non-linearity (since static axial deflection is very large), whereas frequency response analysis is a linear study with small excitation amplitudes. Hydrogel is modelled to be a linear elastic material with an isotropic loss factor of 0.02 (equivalent to ζ_r = 0.01 for all vibration modes). As shown in Figure 4.5, the gel model is fixed at the top face (yellow shaded region) and harmonic perturbation is provided to the fixed end in transverse direction while a domain point probe (red dot in Figure 4.5) measures response at the tip.

The FEM model comparison with experimental results can be seen in Figure 4.6. It can

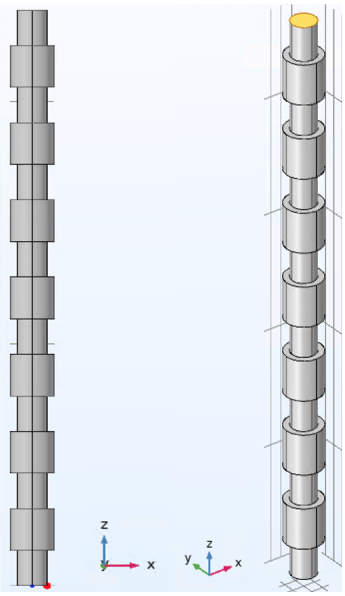

Figure 4.5: COMSOL representation of the periodic hydrogel in 2-D (left) and 3-D (right) orientation.

be observed that COMSOL model agrees well with experimental results when compared to Timoshenko FEM model. Bandgap in Timoshenko FEM model is wider and occurs at a lower frequency. Even though COMSOL model agrees well with experiments, the match is not perfect. Periodic hydrogels can be imperfect due to material inhomogeneities and photo-patterning. The resultant surface imperfections are not accounted in the COMSOL model. Additionally, the COMSOL model also assumes a sharp or step-like transition between the non-swollen and swollen segments which can potentially have an effect on the level of agreement.

4.4 Case Studies

This section discusses different approaches to tune a bandgap in a periodic hydrogel structure. The reprogrammability feature of hydrogels is first explored to study the consistency of bandgap formation and the ability to tune a bandgap by re-programming the length ratio, α of the unit cells. Bandgap formation and variation is further studied for TPMLH concentration and unit cell length ratio variations using different hydrogel samples. The ex-

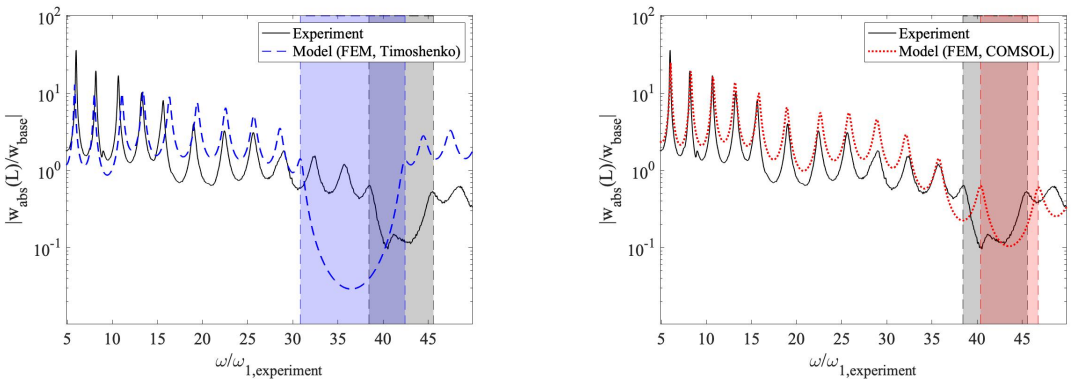

(a) (b)

Figure 4.6: Tip transmissibility comparisons between experiments and (a) Timoshenko beam element and (b) COMSOL based FEM models

perimental trends are compared to the FEM (COMSOL) model predictions and simplified diatomic chain model (chapter 2) is utilized to explain the trends observed in experiments.

4.4.1 Re-programming Hydrogels

Reprogrammibility is an additional feature that these stimuli-responsive hydrogels possess and it can prove to be useful for the purpose of bandgap tuning as one can re-program the same piece of hydrogel to a different geometric periodicity to achieve a desired bandgap. The swollen/periodic hydrogel is first allowed to reset to its homogeneous state and then re-activated by the process discussed in section 4.1. This homogeneous state is achieved by submerging the sample in Poly(ethylene Glycol) (PEG) water solution. This process is followed by submersing the sample in 10 mM NBA water solution (pH = 11.00, conditioned by NaOH). The process is also illustrated in Figure 4.7. This process is repeated 4 times to ensure that previous activation traces are completely eliminated from the sample. The homogeneous sample can be ultimately re-programmed to similar or different geometric characteristics.

In the first attempt, an initial periodic hydrogel sample is re-programmed to achieve identical geometric properties. It can be seen in Figure 4.8 that match in bandgap center frequency and width is excellent between the initially programmed periodic structure and

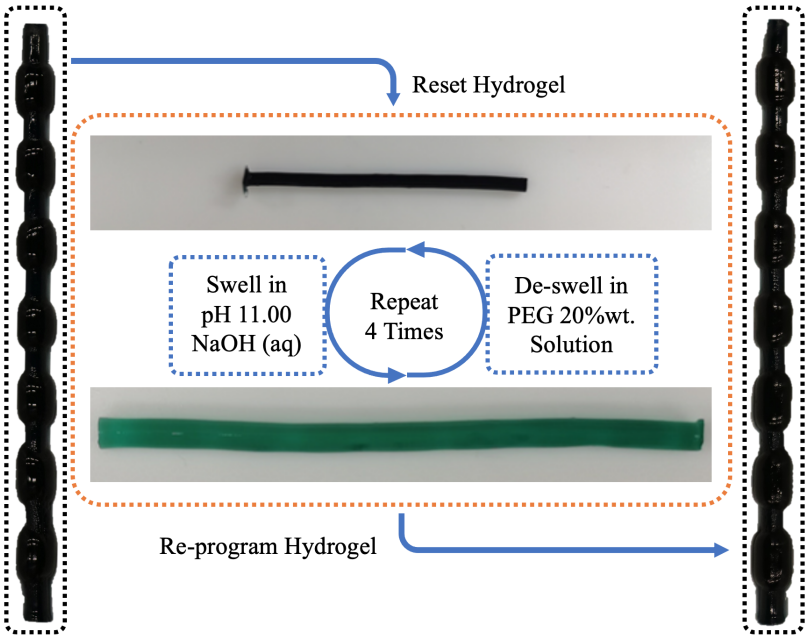

Figure 4.7: Re-programming process for a periodic hydrogel which has identical geometric periodicity upon re-programming. The hydrogel samples can be re-programmed to possess different geometric periodicity by using a photomask of different length proportions.

the re-programmed periodic structure with identical geometry. Despite material inhomogeneity and defects which can be common in these hydrogels, it can be concluded that bandgaps can be easily recreated upon re-programming. In the second attempt, a hydrogel with a unit cell length ratio, α = 1.64 is re-programmed to α = 1.26 and the result is then compared to a new hydrogel sample with $\alpha = 1.26$. It can be seen in Figure 4.9 that the bandgap width and center frequencies match well between the two samples with α = 1.26. The agreement between the re-programmed sample (α = 1.26) and new hydrogel sample (α = 1.26) is not as impressive as the first attempt which focused on exact repetition of the geometry. Unlike exact geometric repetition attempt, unit cell length ratio variation (α = 1.26) would require a photomask of different length proportions, which can introduce variations in the sample when compared to the new hydrogel sample with α = 1.26, potentially explaining the quality of agreement for re-programmed hydrogels.

The shaker test results shown here indicate that it is possible to recreate and/or tune a bandgap using the reprogrammability of hydrogels. However, this process can prove

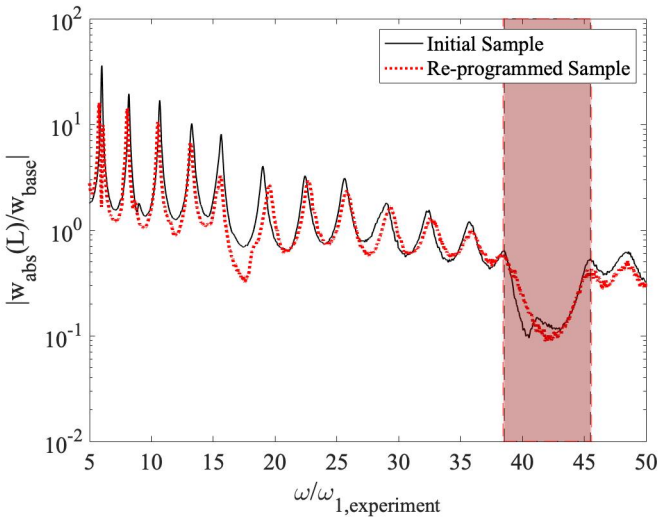

Figure 4.8: Tip transmissibility comparison between periodic hydrogel and its re-programmed version which has been designed to achieve identical geometric specifications.

to be time consuming and erroneous if the samples are not handled with care during re-programming. Upon consideration of these factors and the good repeatability and small deviations between samples, multiple samples of different unit cell length ratios and TPMLH concentrations are instead created simultaneously to make the gel synthesis process efficient.

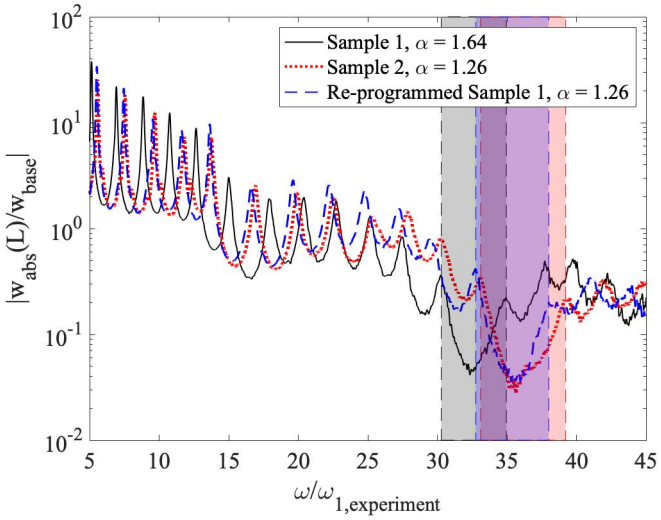

Figure 4.9: Tip transmissibility comparison between periodic hydrogel, sample 2 (α = 1.26) and re-programmed version (α = 1.26) of sample 1 (initial α = 1.64) .

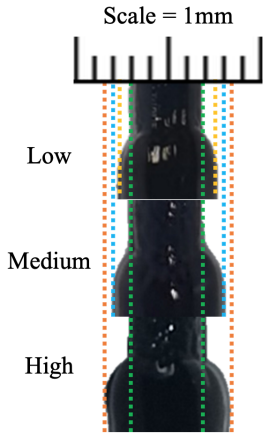

Figure 4.10: Sample comparison for TLMPH concentration variation (TPMLH increases from low to high).

Table 4.1: Hydrogel compositions and dimensional specifications for TLMPH variation

Sample	Low$_{TPMLH}$	Medium$_{TPMLH}$	High$_{TPMLH}$
AAm (M)	3	3	3
Bis (mM)	18	18	18
TPMLH (mM)	38.0	41.5	45.0
d_a (mm)	3.71	3.78	3.74
d_b (mm)	5.05	5.52	5.81
δ	1.36	1.46	1.55
E_a (kPa)	9.90	9.15	8.55
E_b (kPa)	9.60	8.40	6.90
ϵ	1.03	1.09	1.23
L_a (mm)	5.24	5.43	5.47
L_b (mm)	6.87	7.27	7.43
α	1.31	1.34	1.36

Bandgap tuning is studied in experimental settings primarily through variation of two parameters: TPMLH concentration and unit cell length ratio, α. While TPMLH concentration variation alters the chemical composition of the hydrogel and ultimately the level of swelling, unit cell length ratio variation enables change in the hydrogel geometry (can be performed by using a photomask of different window size) while TPMLH concentration remains constant. It can be noticed in Table 4.1 that both diameter (δ) and Young's mod-

ulus (ϵ) ratio increase with TPMLH concentration. The same photomask is used for the photo-activation, however it can also be noticed that samples with higher TPMLH concentration see a slight increase in unit cell length ratio which can be attributed to the increase in localized swelling of the structure in the longitudinal direction. The diameter ratio increase is also evident in Figure 4.10 which compares the samples with different TPMLH concentration (Low = 38 mM, Medium = 41.5 mM, High = 45 mM).

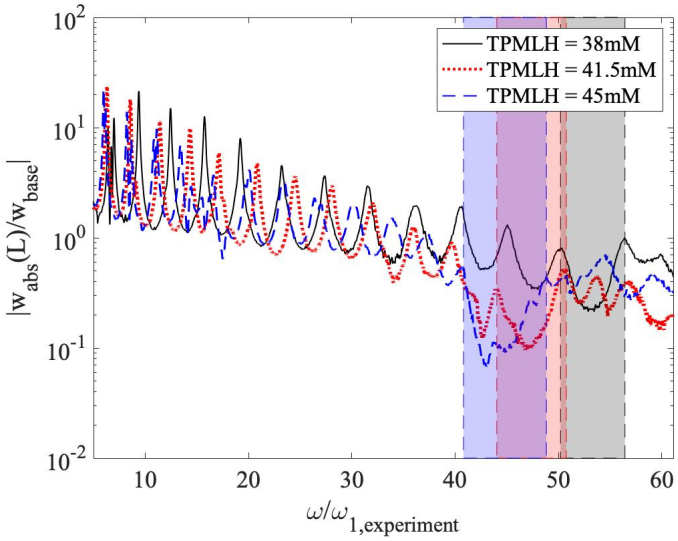

Figure 4.11: Experimental tip transmissibility for periodic hydrogels as TPMLH concentration is varied from 38 mM to 45 mM.

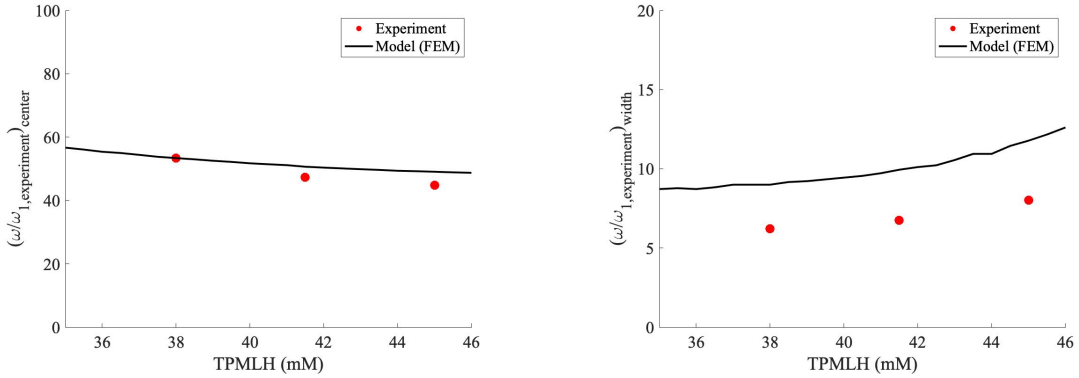

Figure 4.12: Second bandgap (a) center frequency and (b) width comparison between experiment and FEM (COMSOL) as TPMLH concentration is varied from 35 mM to 46 mM.

In Figure 4.11, it can be observed that the bandgap gets wider and shifts to a lower center frequency with increase in TPMLH concentration. It can further be noticed that the quality of attenuation also improves with increase in TPMLH concentration. Similar trends are noticed in FEM model (COMSOL), however the model overestimates both the bandgap center frequency and width. A new 3 sample batch is further created with different unit cell length ratios (α = 1.00, 1.49, and 2.02). The samples of this batch are made with the same chemical composition as sample, "High" in Table 4.1 (TPMLH = 45 mM). However, due to batch-to-batch variations, both diameter and Young's modulus ratio (δ = 1.66 and ϵ = 1.48) vary slightly when compared to Table 4.1.

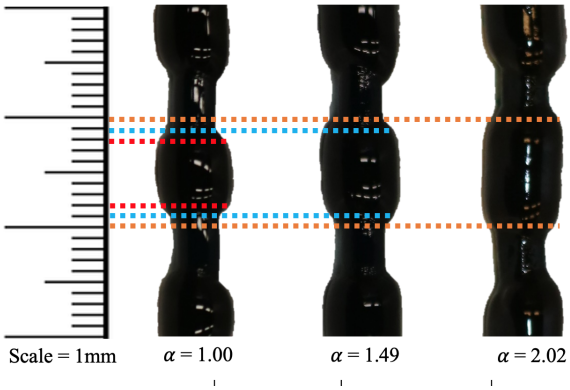

Figure 4.13: Sample comparison for α variation.

In Figure 4.14, it can be observed that the bandgap shrinks and shifts to a lower center frequency with increase in unit cell length ratio. Similar trends are noticed in FEM (COMSOL) model. The model versus experiment comparisons can be seen in Figure 4.15. Unlike TPMLH sweep results, the model underestimates the bandgap width when compared to experiments. In chapter 2 and 3, we noticed that the bandgaps shifted to a higher center frequency with increase in unit cell length ratio, hence contradicting the results shown here. However, the preliminary case studies assumed that the total unit cell length remained constant (total length of the finite periodic structure would remain constant) as we varied the unit cell length ratio. It can be seen in Figure 4.13 and Table 4.2 that the total length of the unit cell increases with unit cell length ratio. Such behavior can again be attributed to

Table 4.2: Hydrogel compositions and dimensional specifications for unit cell length ratio variation

Sample	Low_α	Medium_α	High_α
AAm (M)	3	3	3
Bis (mM)	18	18	18
TPMLH (mM)	45.0	45.0	45.0
d_a (mm)	3.92	3.97	3.99
d_b (mm)	6.50	6.58	6.59
δ	1.66	1.66	1.66
E_a (kPa)	7.35	7.35	7.35
E_b (kPa)	4.95	4.95	4.95
ϵ	1.48	1.48	1.48
L_a (mm)	6.64	5.57	4.85
L_b (mm)	6.66	8.29	9.82
Length of unit cell (mm)	13.30	13.86	14.67
α	1.00	1.49	2.02

the increased localized swelling in the longitudinal direction. A longer activated segment will tend to swell more, hence providing a longer unit cell and ultimately a longer finite periodic structure.

4.4.3 Diatomic Chain Model

In the previous sections, we noticed that the bandgap widens and shifts to a lower center frequency with increase in TPMLH concentration, whereas increase in unit cell length ratio (α) can shrink the bandgap while shifting it to a lower center frequency. These trends can be interpreted using the simplified diatomic chain model that we discussed in chapter 2. The variations in TPMLH concentration and unit cell length ratio ultimately fluctuate the unit cell mass and stiffness ratios which are fundamentally responsible for bandgap formation in periodic structures. For a structure under bending vibration, the equivalent mass and stiffness ratios can be given by

$$\mu = \delta^2 \alpha, \qquad \kappa = \frac{\delta^4}{\epsilon \alpha^3}. \tag{4.2}$$

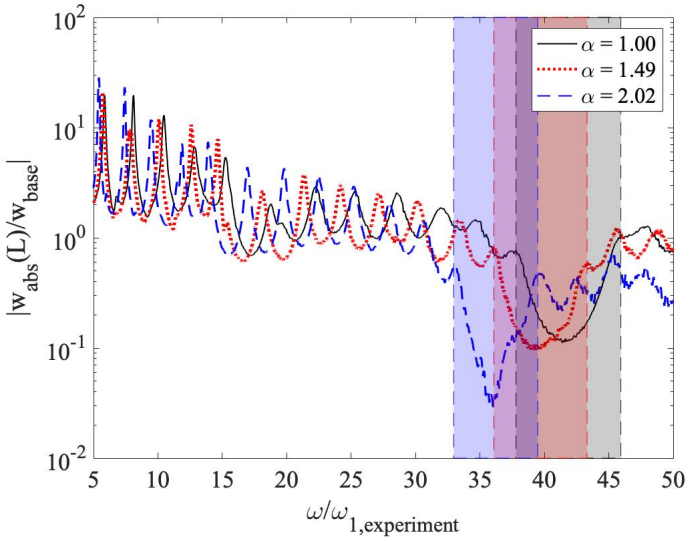

Figure 4.14: Experimental tip transmissibility for periodic hydrogels as α is varied from 1.00 to 2.02.

To analyze the experimental trends using the diatomic chain model, Equation 4.2 can be used to solve for the mass(μ) and stiffness ratios(κ) of the unit cell. Table 4.2 and 4.3 provide the equivalent mass and stiffness ratios for the experimentally tested samples.

Table 4.3: Equivalent mass and stiffness ratios for the unit cells of the TPMLH variation samples. The bandgap center frequencies and widths are calculated using diatomic chain model.

Sample	TPMLH (mM)	μ	κ	Ω_{center}	Ω_{width}
Low_{TPMLH}	38.0	3.18	1.48	1.22	0.73
Medium_{TPMLH}	41.5	3.83	1.61	1.21	0.84
High_{TPMLH}	45.0	4.46	1.74	1.21	0.92

It can be seen that increase in TPMLH concentration results in higher mass and stiffness ratios which ultimately provide a wider bandgap at a lower center frequency. However, for the amount of increase in mass and stiffness ratios due to TPMLH variation, diatomic chain model predicts a negligible reduction in bandgap center frequency. On the other hand, higher unit cell length ratios result in higher mass but lower stiffness ratios which ultimately provide a narrower bandgap at a lower center frequency. Similar trends can also be observed in Figure 4.16.

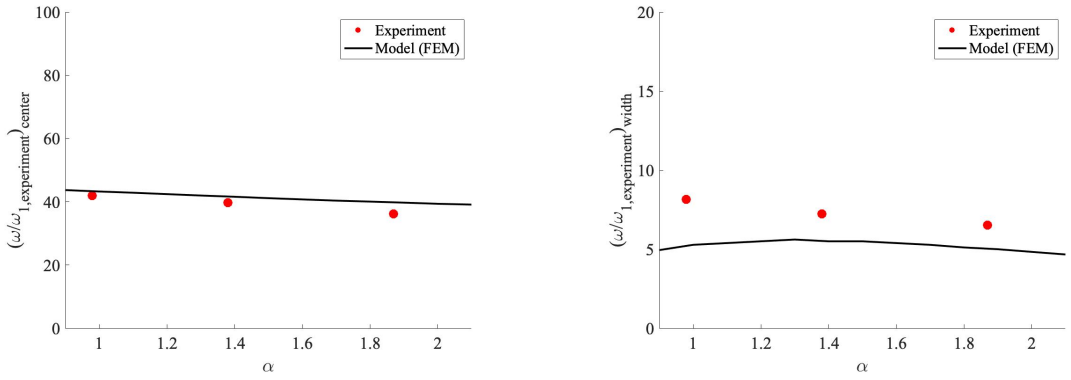

Figure 4.15: Second bandgap (a) center frequency and (b) width comparison between experiment and FEM (COMSOL) as α varies from 0.9 to 2.1.

Table 4.4: Equivalent mass and stiffness ratios for the unit cells of the length ratio variation samples. TPMLH concentration is 45mM for all three samples.

Sample	α	μ	κ	Ω_{center}	Ω_{width}
Low_α	1.00	2.76	5.05	1.85	1.68
Medium_α	1.49	4.09	1.54	1.18	0.84
High_α	2.02	5.52	0.60	0.89	0.75

4.5 Summary and Conclusions

This chapter focuses on the experimental efforts to study bandgap formation and tunability in TPMLH hydrogel-based hydrogel structures. The structural response is measured at the free end of the cantilevered hydrogel structure while the fixed base is excited by a low amplitude rectangular noise signal. Bandgaps are clearly evident in the tip transmissibility plots for periodic hydrogel structures. A COMSOL finite element model is also developed to consider external factors such as static deflection due to the presence of gravity. It is noticed that unlike Timoshenko FEM model, COMSOL finite element model matches well with the experimental results.

TPMLH concentrations and unit cell length ratios are further varied to examine the tunability aspect of the observed bandgap. Significant variations are observed in experimental bandgap width and center frequency. The experimental bandgap trends are then compared

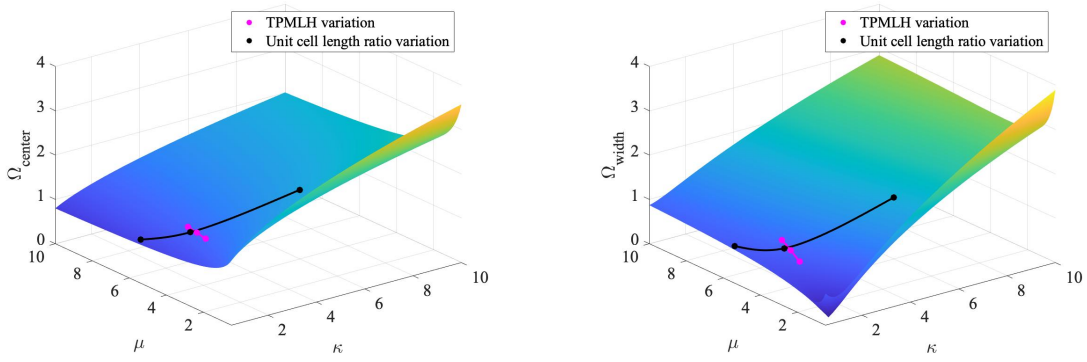

(a) (b)

Figure 4.16: (a) Bandgap center frequency and (b) width variation in diatomic chain model. The overlaid scatter points represent the bandgap widths and center frequencies for the experimental case studies as predicted by the diatomic chain model.

to a much simpler diatomic chain model. While the diatomic model bandgap widths and center frequencies carry little quantitative relevance, they provide an understanding of how bandgaps occur and vary in periodic structures. Trends identical to experiments are noticed when diatomic model bandgap width and center frequencies are evaluated using the equivalent mass and stiffness ratios of the hydrogel samples used in the experiments. The trend agreement can help us come to a conclusion that the experimental variations in the bandgap width and center frequency are ultimately a consequence of the change in mass and stiffness ratios of the unit cell. This comparison also helps us conclude that despite the presence of static deflection in the samples which jeopardizes the periodicity of the structure, these periodic hydrogels are capable of following the fundamental principles of bandgap formation in periodic structures.

CHAPTER 5
CONCLUSION AND NEXT STEPS

This thesis successfully demonstrates bandgap formation and tuning in stimuli-responsive hydrogel-based periodic structures. Analytical and FEM models are first created in efforts to effectively study the formation and tuning of bandgaps with respect to parameters such as diameter, Young's modulus, and unit cell length ratio. Chapter 2 provides the detailed approach for performing dispersion analysis on the unit cell of an infinite periodic structure. Transfer matrix method is utilized to setup the eigenvalue problem and ultimately create dispersion curve plots which can reveal the location and width of bandgaps in frequency domain. Chapter 3 focuses on the finite element method approach which is employed to analyze the bandgap formation in periodic structures with finite number of unit cells. An infinite periodic structure will entirely prohibit wave propagation within the bandgap, however as seen in Figure 3.5, bandgap attenuation in finite periodic structure depends on the number of unit cells. Two very common beam theories: Euler-Bernoulli and Timoshenko are used throughout chapter 2 and 3 to model bandgaps in periodic structures under bending vibrations. Due to the low Young's modulus and low unit cell aspect ratio, shear deformation and rotational inertia effects are non-negligible in periodic hydrogel structures. As a result, Euler-Bernoulli beam models (neglects shear deformation and rotational inertia effects) overestimate both the width and location of bandgaps when compared to Timoshenko beam models. Variations in parameters such as TPMLH concentration would alter diameter, Young's modulus, and unit cell length ratio simultaneously, hence it is not entirely known which parameter contributes the most to bandgap tuning. While initial dispersion and FEM models do not match the experimental results as well as COMSOL based finite element model, they allow us to study bandgap tuning in periodic structures for independent variations in diameter, Young's modulus, and unit cell length

ratio. Chapters 2 and 3 conclude that increase in diameter ratio results in wider bandgaps at higher center frequencies, whereas larger Young's modulus ratios yield wider bandgaps at lower center frequencies. Increase in unit cell length ratio on the other hand, produces narrower bandgaps which occur at a marginally higher center frequency.

Chapter 4 focuses on linear shaker vibration tests which are performed on TPMLH based hydrogels. In efforts to match the experimental results, additional factors such as static deflection (due to gravitational body loads) is further considered in a COMSOL based finite element model. A good agreement is found between the experiments and COMSOL based finite element model. Bandgap variations in hydrogel samples with different TPMLH concentrations and unit cell length ratios are further studied experimentally. It is observed that higher TPMLH concentrations yield wider bandgaps at lower center frequencies, whereas higher unit cell length ratios produce narrower bandgaps at lower center frequencies. Identical trends are noticed in the finite element model (COMSOL) and the simplified diatomic chain model, hence implying that the experimental trends are a ultimately a result of variations in unit cell mass and stiffness ratios. It is ultimately concluded that despite of the external factors such as static deflection and surface defects in hydrogel samples, hydrogel-based periodic structures are still capable of following the basic principles of wave propagation and bandgap formation in periodic structures.

In the next steps to the efforts presented in this thesis, several modelling techniques can be considered to improve the match between experiments and models. Error in the measurements of hydrogel dimensions and material properties has to be further considered in the models. Both dimensions and Young's modulus measurements utilize image processing techniques which can introduce an uncertainty in the measurements of these physical parameters, and consequently in the model's bandgap estimations. Surface irregularities and transition zones were neglected for all the models discussed in this thesis and they can be a potential source of discrepancy. A comprehensive reconstruction of the structure geometry using high definition images can help capture the remaining geometric details. Addition-

ally, inclusion of static deflection and resulting non-linearities (due to static deflection) in conventional Timoshenko beam theory based model can help with the formulations of the analytical predictions for bandgaps in hydrogel structures. Having demonstrated bandgap formation and tuning in simple periodic structures, more complex metamaterial concepts can be further explored in 2-D and 3-D hydrogel-based structures. Adding hard inclusions in hydrogel structures can also be considered to explore an innovative approach of bandgap formation.

REFERENCES

[1] L. Brillouin, *Wave propagation in periodic structures*. Dover, 1946.

[2] Z. Liu, X. Zhang, Y. Mao, Y. Zhu, Z. Yang, C. Chan, and P. Sheng, "Locally resonant sonic materials", *American Association for the Advancement of Science*, vol. 289, pp. 1734–1736, 2000.

[3] C. Sugino, S. Leadenham, M. Ruzzene, and A. Erturk, "On the mechanism of bandgap formation in locally resonant finite elastic metamaterials", *Journal of Applied Physics*, vol. 120, 2016.

[4] L. Raghavan and A. Phani, "Local resonance bandgaps in periodic media: Theory and experiment", *The Journal of the Acoustical Society of America*, vol. 134, pp. 1950–1959, 2013.

[5] C. Kittel, *Introduction to solid state physics*. Wiley, 1986.

[6] Rayleigh, "Xvii.on the maintenance of vibrations by forces of double frequency, and on the propagation of waves through a medium endowed with a periodic structure", *Philosophical Magazine Series 5*, vol. 24, pp. 145–159, 1887.

[7] D. Mead, "Wave propagation in continous periodic structures: Research contributions from southampton 1964-1995", *Journal of Sound and Vibrations*, vol. 190, pp. 495–524, 1996.

[8] C. Elachi, "Waves in active and passive periodic structures: A review", *Proceedings of the IEEE*, vol. 64, pp. 1666–1698, 1976.

[9] A. Movchan, N. Movchan, and S. Haq, "Localised vibration modes and stop bands for continuous and discrete periodic structures", *Materials Science and Engineering: A*, vol. 431, pp. 175–183, 2006.

[10] L. Brinson, "One-dimensional constitutive behavior of shape memory alloys: Thermomechanical derivation with non-constant material functions and redefined martensite internal variable", *Journal of Intelligent Material Systems and Structures*, vol. 4, pp. 229–242, 1993.

[11] V. Sousa, D. Tan, C. Marqui Jr., and A. Erturk, "Tunable metamaterial beam with shape memory alloy resonators: Theory and experiment", *Applied Physics Letters*, vol. 113, 2018.

[12] Y. Chen, G. Huang, and C. Sun, "Band gap control in an active elastic metamaterial with negative capacitance piezoelectric shunting", *Journal of Vibrations and Acoustics*, vol. 136, 2014.

[13] K. Yi and M. Collet, "Broadening low-frequency bandgaps in locally resonant piezoelectric metamaterials by negative capacitance", *Journal of Sound and Vibration*, vol. 493, 2021.

[14] C. Sugino, M. Ruzzene, and A. Erturk, "Digitally programmable resonant elastic metamaterials", *Physical Review Applied*, vol. 13, 2020.

[15] N. Nadkarni, C. Daraio, and D. Kochmann, "Dynamics of periodic mechanical structures containing bistable elastic elements: From elastic to solitary wave propagation", *Physics Review E*, vol. 90, 2014.

[16] N. Nadkarni, A. Arrieta, C. Chong, D. Kochmann, and C. Daraio, "Unidirectional transition waves in bistable lattices", *Physics Review Letters*, vol. 116, 2016.

[17] Y. Xia, M. Ruzzene, and A. Erturk, "Dramatic bandwidth enhancement in nonlinear metastructures via bistable attachments", *Applied Physics Letters*, vol. 114, 2019.

[18] S. Ning, Z. Yan, D. Chu, H. Jiang, Z. Liu, and Z. Zhuang, "Ultralow-frequency tunable acoustic metamaterials through tuning gauge pressure and gas temperature", *Extreme Mechanics Letters*, vol. 44, 2021.

[19] S. Alan, A. Allam, and A. Erturk, "Programmable mode conversion and bandgap formation for surface acoustic waves using piezoelectric metamaterials", *Applied Physics Letters*, vol. 115, 2019.

[20] G. M. and M. Lapine, "Tuning of a nonlinear metamaterial band gap by an external magnetic field", *Physical Review B*, vol. 70, 2004.

[21] Y. Li and Y. Xu, "Tuning and switching of band gap of the periodically undulated beam by the snap through buckling", *American Institute of Physics Advances*, vol. 7, 2017.

[22] T. Hoare and D. Kohane, "Hydrogels in drug delivery: Progress and challenges", *Polymers*, vol. 49, pp. 1993–2007, 2008.

[23] J. Drury and D. Mooney, "Hydrogels for tissue engineering: Scaffold design variables and applications", *Biomaterials*, vol. 24, pp. 4337–4351, 2003.

[24] S. Naficy, R. Gately, R. Gorkin III, H. Xin, and G. Spinks, "4d printing of reversible shape morphing hydrogel structures", *Macromolecular Materials and Engineering*, vol. 302, 2017.

[25] A. Gladman, E. Matsumoto, R. Nuzzo, L. Mahadevan, and J. Lewis, "Biomimetic 4d printing", *Nature Materials*, vol. 15, pp. 413–418, 2016.

[26] Y. Lai and Y. Hu, "Probing the swelling-dependent mechanical and transport properties of polyacrylamide hydrogels through afm-based dynamic nanoindentation", *Royal Society of Chemistry*, vol. 14, 2018.

[27] B. Wang, A. Moura, J. Chen, A. Erturk, and Y. Hu, "Characterization of hydrogel structural damping", *Extreme Mechanics Letters*, vol. 40, 2020.

[28] T. Park and A. Hoffman, "Deswelling characteristics of poly(n-isopropylacrylamide) hydrogel", *Journal of Applied Polymer Science*, vol. 52, pp. 85–89, 1994.

[29] D. Beebe, J. Moore, J. Bauer, Q. Yu, R. Liu, C. Devadoss, and B. Jo, "Functional hydrogel structures for autonomous flow control inside microfluidic channels", *Nature*, vol. 404, pp. 588–590, 2000.

[30] S. Jeon, A. Hauser, and R. Hayward, "Shape-morphing materials from stimuli-responsive hydrogel hybrids", *American Chemical Society*, vol. 50, pp. 161–169, 2017.

[31] D. Morales, E. Palleau, M. Dickey, and O. Velev, "Electro-actuated hydrogel walkers with dual responsive legs", *Soft Matter*, vol. 10, pp. 1235–1430, 2014.

[32] M. Irie and D. Kunwatchakun, "Photoresponsive polymers. 8. reversible photostimulated dilation of polyacrylamide gels having triphenylmethane leuco derivatives", *Macromolecules*, vol. 19, pp. 2476–2480, 1986.

[33] J. Chen, J. Huang, H. Zhang, and Y. Hu, "A photoresponsive hydrogel with enhanced photoefficiency and the decoupled process of light activation and shape changing for precise geometric control", *American Chemical Society*, vol. 12, pp. 38 647–38 654, 2020.

[34] M. Hussein, M. Leamy, and M. Ruzzene, "Dynamics of phononic materials and structures: Historical origins, recent progress,and future outlook", *Applied Mechanics Review*, vol. 66, 2014.

[35] L. Meirovitch, *Principles and techniques of vibrations*. Prentice-Hall, 1997.

[36] D. Yu, J. Wen, H. Zhao, Y. Liu, and X. Wen, "Vibration reduction by using the idea of phononic crystals in a pipe-conveying fluid", *Journal of Sound and Vibration*, 2008.

[37] T. Chen and L. Wang, "Suppression of bending waves in a periodic beam with timoshenko beam theory", *Acta Mechanica Solida Sinica*, vol. 26, 2011.

[38] G. Cowper, "The shear coefficient in timoshenko's beam theory", *Journal of Applied Mechanics*, vol. 33, no. 2, pp. 335–340, 1966.

[39] A. Erturk and D. Inman, "Issues in mathematical modeling of piezoelectric energy harvesters", *Smart Materials and Structures*, 2008.

[40] C. Junior, A. Erturk, and D. Inman, "An electromechanical finite element model for piezoelectric energy harvester plates", *Journal of Sound and Vibration*, vol. 327, pp. 9–25, 2009.

[41] R. Davis, R. Henshell, and G. Warburton, "A timoshenko beam element", *Journal of Sound and Vibration*, vol. 22, no. 4, pp. 475–487, 1972.

[42] K. Kapur, "Vibrations of a timoshenko beam, using finite-element approach", *The Journal of the Acoustical Society of America*, vol. 40, no. 5, pp. 1058–1063, 1966.